Magdalena Truger, BSc

The Surface Induced Crystal Structure of 6,6'-Dibromoindigo: Origin and Stability

MASTER'S THESIS

to achieve the university degree of
Diplom-Ingenieur

Master's degree programme of
Technical Physics

submitted to
Graz University of Technology

Supervisor
Ao.Univ.-Prof. Dipl.-Ing. Dr.techn. Roland Resel
Institute of Solid State Physics
Graz University of Technology

Graz, September 2015

AFFIDAVIT

I declare that I have authored this thesis independently, that I have not used other than the declared sources/resources, and that I have explicitly indicated all material which has been quoted either literally or by content from the sources used. The text document uploaded to TUGRAZonline is identical to the present master‘s thesis dissertation.

Date

Signature

Acknowledgement

First of all, I would like to thank my supervisor Roland Resel for all his support and encouragement during my thesis. He made it possible for me to perform synchrotron measurements at the ESRF in Grenoble, attend the NESY Winterschool in Altaussee and visit Charles University Prague.
I would like to thank Ingo Salzmann, Dominik Kriegner and Christian Röthel for their help and lively discussions during the beamtime at ESRF and beyond. Furthermore, I wish to thank Anna Coclite for preparing the polymer substrates, Clemens Simbrunner, Rizwan Ahmed, Mihai Irimia-Vladu and Eric Głowacki for preparing samples by hot wall epitaxy, Josef Simbrunner for the analytical calculation of the unit cells, Otello M. Roscioni for calculating the crystal structure solution, and Vaclav Holy for inviting me to Prague and the interesting discussions.
Moreover, I would like to thank all members of the institute, especially Elisabeth Stern, Birgit Kunert and Harald Kerschbaumer for assisting with various problems. Special thanks go to my colleagues of our working group Stefan Pachmajer, Andrew Jones, Benedikt Schrode, Paul Christian, Katrin Unger and Georg Urstöger. Thank you for all your help throughout my thesis and always having an open ear for my questions and discussions. I really enjoyed sharing an office with you.
I would like to mention all my friends I met during my studies, especially Ramona Köppl, Nina Feldhofer, Harald Thommesen, Alexandra Müller, Nina Fleischmann, Tanja Pelzmann and Christof Jell. Thank you for all your support and friendship, without you I would not have gotten so far. Likewise, I wish to thank Elke Müller, Niki Penkoff, and Viktoria Schichl and her family for always finding the right words of encouragement.
Last, but by no means least, I would particularly like to thank my whole family for enabling me to study and, more importantly, for their unconditional support throughout my education.

Abstract

6,6'-Dibromoindigo (Tyrian purple) has been known as a natural dye for centuries, but has recently become interesting for its semiconducting properties. Semiconductors based on natural materials provide a way to build sustainable, biodegradable and environmentally stable electronic devices. Tyrian purple has been used to build transistors, however, the crystal structure of Tyrian purple in thin films, which build the active layer of electronic devices, has not yet been solved. Within this thesis, the crystallographic properties of thin films of Tyrian purple are investigated. The surface induced phase of Tyrian purple on different substrates is studied by X-ray diffraction techniques. X-ray reflectivity measurements show, that no continuous monolayer, but rather islands are formed. A dependence of the unit cell on the film thickness is observed for samples on silicon oxide. The unit cell is triclinic with one molecule per cell, which is considerably different from the known crystallographic structure solved from macroscopic single crystals. The crystal structure solution for the surface induced phase was calculated using molecular dynamics simulations. The molecules pack in parallel stacks of standing molecules. In addition, there are lying molecules on polymer substrates. The unit cell parameters also vary slightly with the surface energy of the substrates, especially the out-of-plane parameter c and, thus, the unit cell volume, which is in a range between $332\,\text{Å}^{-3}$ and $355\,\text{Å}^{-3}$. Additionally, the thermal stability of the surface induced phase is studied. A phase transition from the surface induced phase to the bulk phase is observed at 210 °C. After cooling down, the bulk phase remains, which shows that the bulk phase is indeed rather the stable polymorph, whereas the surface induced phase is rather metastable.

Kurzfassung

6,6'-Dibromoindigo (Tyrian Purple, Purpur) ist seit vielen Jahrhunderten als natürlicher Farbstoff bekannt und kürzlich auch aufgrund seiner halbleitenden Eigenschaften interessant geworden. Halbleitende Materialien natürlichen Ursprungs bieten eine Möglichkeit nachhaltige, biologisch abbaubare und unter Umgebungsbedingungen stabile elektronische Halbleiter-Bauelemente herzustellen. Tyrian Purple ist bereits in Transistoren verbaut worden, allerdings ist die Kristallstruktur von Tyrian Purple in dünnen Schichten, wie sie in elektronischen Bauelementen gebraucht werden, noch nicht gelöst. In dieser Arbeit werden die kristallographischen Eigenschaften von Tyrian Purple in dünnen Filmen untersucht. Die oberflächeninduzierte Phase von Tyrian Purple auf verschiedenen Substraten wird mittels Röntgenbeugung untersucht. Es wird gezeigt, dass keine durchgängigen Monolagen gebildet werden, sondern Inselwachstum auftritt. Eine Abhängigkeit der Einheitszelle von der Schichtdicke wird auf Siliziumoxid-Substraten beobachtet. Die Einheitszelle ist triklin mit einem Molekül pro Zelle, und unterscheidet sich somit signifikant von der Einkristallstruktur. Die Struktur der oberflächeninduzierten Phase wird mittels Molecular Dynamics Simulationen gelöst. Die Moleküle packen in parallelen Stapeln stehender Moleküle, zusätzlich wurde auf Polymersubstraten eine liegende Orientierung gefunden. Die Einheitszellenparameter variieren mit der Oberflächenenergie der Substrate, insbesondere der Parameter c, und somit auch das Volumen, welches in einem Bereich von $332\,\text{Å}^{-3}$ bis $355\,\text{Å}^{-3}$ liegt. Weiters wird die thermische Stabilität der oberflächeninduzierten Phase untersucht. Ein Phasenübergang von der oberflächeninduzierten Phase zur Einkristallstruktur wurde bei 210 °C beobachtet. Während des Abkühlens blieb die Einkristallphase stabil, daher ist diese, wie erwartet, die thermodynamisch stabile, während die oberflächeninduzierte Phase metastabil ist.

Contents

1 Introduction **1**

1.1 6,6'-Dibromoindigo (Tyrian purple) 1

1.1.1 History 1

1.1.2 Physical chemistry 2

1.1.3 The crystal bulk structure 3

1.1.4 Tyrian purple as organic semiconductor 4

1.2 Polymorphism 4

1.3 Crystallization on surfaces 5

1.4 Crystal structure solution 6

1.4.1 Crystallography 6

1.4.2 X-ray diffraction 8

2 Experimental Techniques **13**

2.1 Sample preparation 13

2.1.1 Thermal vapor deposition 13

2.1.2 Hot wall epitaxy 14

2.2 X-ray diffraction 15

2.2.1 Specular X-ray diffraction 15

2.2.2 X-ray reflectivity 17

2.2.3 Grazing incidence X-ray diffraction 19

3 Substrates and Samples **23**

3.1 Substrate preparation 23

3.1.1 Silicon oxide substrates 23

3.1.2 Polymer substrates 23

3.2 Substrate characterization 25

3.2.1 Contact angle measurements 25

3.2.2 Atomic force microscopy 26

3.3 Polymer substrates 27
3.3.1 EGDMA (Ethylene glycol dimethacrylate) 27
3.3.2 HMDSO (Hexamethyldisiloxane) 28
3.3.3 PFDA (1H,1H,2H,2H-perfluorodecyl acrylate) 30
3.4 Surface energies of the substrates 32
3.5 Sample overview 33

4 Results and Discussion 35
4.1 Bulk phase and surface induced phase 35
4.2 Surface induced phase on SiO_2 39
4.2.1 On conventionally cleaned SiO_2 39
4.2.2 On plasma etched SiO_2 47
4.2.3 Comparison 53
4.3 Surface induced phase on other substrates 56
4.3.1 EGDMA (Ethylene glycol dimethacrylate) 56
4.3.2 HMDSO (Hexamethyldisiloxane) 58
4.3.3 PFDA (1H, 1H, 2H, 2H,-perfluorodecyl acrylate) . . . 61
4.4 Surface energy dependence of the surface induced phase . . . 62
4.5 Thermal stability 65

5 Conclusion 69

List of Figures 72

List of Tables 73

List of Abbrevations 75

Bibliography 76

1 Introduction

Recently, indigoids and other organic dye molecules have become interesting because of their semiconducting properties [1,2]. Organic semiconductors are a cheap and easy way to build electronic devices and therefore of high interest in semiconductor research. With the increasing amount of electronics used and thus increasing electronic waste, semiconductors based on natural materials would allow for sustainable and biodegradable electronic devices, which are environmentally stable [3,4]. The semiconducting layer in electronic devices is usually very thin. The properties of these thin films might be quite different from those of the bulk. Within this thesis, thin films of 6,6'-dibromoindigo are investigated in terms of crystal structure and thermal stability.

1.1 6,6'-Dibromoindigo (Tyrian purple)

1.1.1 History

Indigo and its derivative 6,6'-dibromoindigo (Tyrian purple) have been known for about 4000 years. These dyes were produced from organic precursors from plant origin (indigo) and animal origin (Tyrian purple) respectively, in what may have been one of the world's first chemical syntheses by mankind [3].
About 1500 BC ancient Phoenicians discovered that secretions produced by Mediterranean sea snails would dye textiles. Soon the city of Tyre, Lebanon, became the center of the dyeing industry, resulting in the name Tyrian purple for 6,6'-dibromoindigo. The extraction process was highly laborious with many thousand snails being necessary to dye one cloth. Therefore, the color purple was reserved for the wealthy and powerful. For example, in

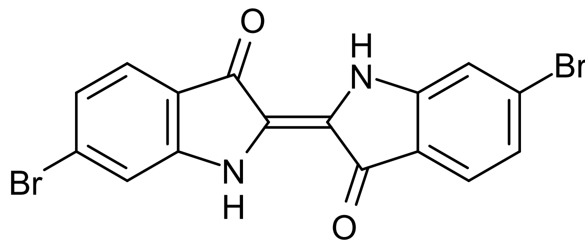

Figure 1.1: Chemical structure of Tyrian purple (6,6'-dibromoindigo)

Ancient Rome there were rules, which person was allowed to wear purple stripes on a toga [3].
In the beginning of the 19th century, it was discovered that Tyrian purple is closely related to indigo. In 1909, Paul Friedländer found the chemical structure of Tyrian purple to be 6,6'-dibromoindigo ($C_{16}H_8N_2O_2Br_2$) [5]. The chemical structure is shown in Figure 1.1. Soon after, Tyrian purple and other indigo derivatives were synthesized for the first time [6].

1.1.2 Physical chemistry

An important property of Tyrian purple and other indigo derivatives is the strong hydrogen bonding. Hydrogen bonds form between oxygen and hydrogen atoms, thus reinforcing the planarity of the molecule. These are also the reason why Tyrian purple exists only in its *trans* form, since hydrogen bonding is influencing the molecular conformation. For example, the intramolecular distance between the amine hydrogen and the oxygen is only 2.5 Å compared to 2.8 Å for only van der Waals bonding. Furthermore, there are also hydrogen bonds between two neighboring molecules which affect the molecular packing and the crystal structure.
The hydrogen bonds in Tyrian purple are further responsible for the high stability of the molecule. Cloth dyed with Tyrian purple has retained its color over the centuries but also electronic devices built with Tyrian purple are highly stable and can even be operated at ambient conditions [3,7].

1.1.3 The crystal bulk structure

The crystal bulk structure was solved in 1979 [8]. It is monoclinic with two atoms in the unit cell. Table 1.1 shows the unit cell parameters available in literature. The crystal structure is depicted in Figure 1.2. The two molecules in the cell are tilted with respect to each other, thus giving a herringbone structure. Each molecule is hydrogen bonded to four neighbors as well as π-stacked to molecules of the same column. The hydrogen bonds have an influence on the structure since they are directional and have a shorter bond length than van der Waals bonds.

Table 1.1: Crystal bulk structure of Tyrian purple: unit cell parameters from literature [8,9]

	[8]	[9]
space group	$P2_1/a$	$P2_1/c$
a [Å]	11.5	12.609
b [Å]	4.85	4.842
c [Å]	12.6	11.611
β [°]	104.0	104.42
V [Å^3]	681.89	686.553

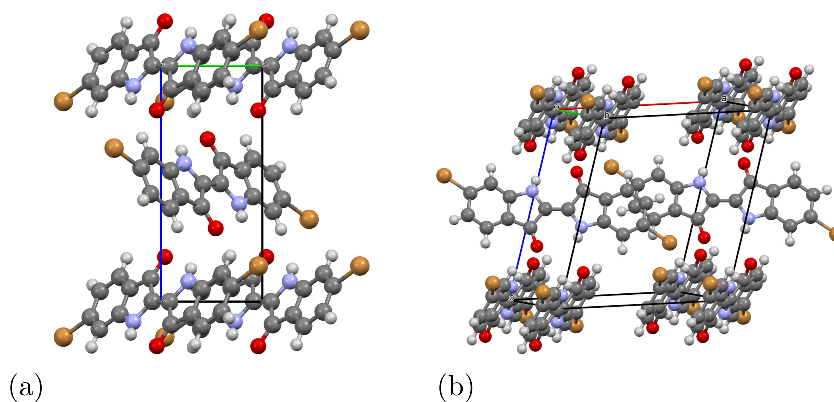

(a) (b)

Figure 1.2: Crystal bulk structure of Tyrian purple [9]
(a) view along the a axis, (b) view along arbitrary direction

1.1.4 Tyrian purple as organic semiconductor

With its aromatic rings and the double bond at the center of the molecule, Tyrian purple is a conjugated molecule. Together with the π-stacking of parallel molecules, this determines the semiconducting properties of the molecule [7].
Good charge carrier properties have been reported for thin films of Tyrian purple. Tyrian purple and other indigoids show ambipolar behavior. In transistors, high hole and electron mobilities of $0.22\,\mathrm{cm^2/V\,s}$ and $0.03\,\mathrm{cm^2/V\,s}$ have been observed [1,7].

1.2 Polymorphism

For the preparation of electronic devices, thin films of Tyrian purple are required. However, in thin films, Tyrian purple can not only form the known monoclinic crystal phase, but also a surface induced crystal phase different from the bulk phase [4,10].
The ability to crystallize in different crystal structures is known as polymorphism. This phenomenon was first recognized in 1823 by Eilhard Mitscherlich [11]. Materials with the same chemical composition can form different crystal structures or even be amorphous. This results in different properties of the material, such as mechanical, optical or electrical, which then depend only on the different structures [12]. Therefore, there is great interest in finding and characterizing polymorphic structures. Especially in organic semiconductor research, it is of high importance to understand the polymorphism of the semiconductor in thin films which build the active layer of electronic devices. The molecular conformation as well as the molecular packing have a great influence on the charge carrier mobility and thus on the performance of the device [13,14].
However, the origin of polymorphism is still not fully understood. It is difficult to predict whether a material has polymorphic forms and which structure it will exhibit [15].
Mostly, X-ray diffraction techniques are used to determine the crystal structure of polymorphs. By comparing measured diffraction patterns, it can be

determined if one or more phases are present. If the patterns are very similar, softwares can be used to decide whether the structures are the same or polymorphic [16]. Other techniques to investigate crystal polymorphism include hot stage microscopy, differential scanning calorimetry, thermogravimetric analysis, solid state nuclear magnetic resonance spectroscopy and Raman spectroscopy [15].

The conditions during crystal growth often determine the nucleation process and subsequently which polymorph is formed. For example, the temperature, choice of solvent, pressure and crystallization rate can influence the crystal structure [15]. However, also changing parameters like temperature or pressure for an already grown crystal can cause a change in the crystal structure [12].

When more than one crystal structure is possible for a material, the structure with the lowest free energy at given conditions is the stable one. However, also more than one crystal structure can be found coexisting at the same time with the other structures being metastable [17].

1.3 Crystallization on surfaces

When crystallizing thin films on a substrate, additional polymorphic forms can appear [18–20]. These are typically found only in thin films and can not form a free standing crystal [21]. They change to the thermodynamically stable bulk phase at a certain film thickness [18,22]. Figure 1.3 shows a schematic drawing illustrating that the crystal structure of a thin film on a substrate can be significantly different from the single crystal bulk phase.

These thin film crystal structures are often called surface induced phases because the substrate they are crystallized on has a strong impact on the structure. By choosing specific substrate properties, the polymorphism of the film can be influenced. For example, the substrate temperature during film preparation, the substrate chemistry, reactivity or roughness are factors which influence the crystal structure of the film [13].

The structure of thin films depends not only on the substrate but also on the crystallization conditions. The choice of solvent for the film preparation may influence the final structure. If the evaporation rate is high, the

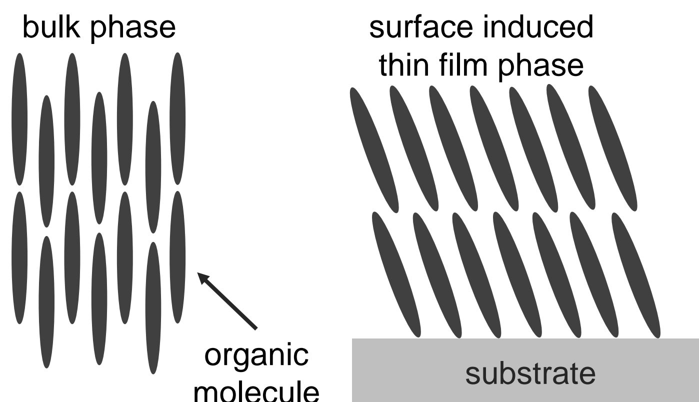

Figure 1.3: Schematic drawing of the single crystal bulk phase (left) versus the surface induced phase (right)

crystallization speed is high as well (low induction time). In this case, the thin film formation happens far from equilibrium and metastable crystal structures are more likely to appear. For low crystallization speeds (large induction time) the crystal bulk phase is preferred [21].
Because of the small film thickness, special surface sensitive X-ray diffraction techniques are required to analyze the crystal structure. These will be introduced in section 1.4.2.

1.4 Crystal structure solution

This section as well as the general parts on X-ray diffraction techniques (section 2.2) are based on the textbooks by Weißmantel [12], Kittel [23], Bennet [24], Birkholz [25], and Schwarzenbach [26] and the lecture notes to *X-ray physics* [27].

1.4.1 Crystallography

In a crystal, all atoms are arranged periodically. This periodic repetition on a microscopic level determines the mechanical, optical and electrical properties of the material on a macroscopic scale.
The periodic arrangement within a crystal can be described by a translational lattice. Starting from one lattice point, three vectors **a**, **b** and **c** can

be defined so that any other lattice point can be described by

$$\mathbf{R} = n_1\mathbf{a} + n_2\mathbf{b} + n_3\mathbf{c} \tag{1.1}$$

with n_1, n_2 and n_3 integers.
These three vectors span a parallelepiped, which is called the primitive unit cell if the volume $V = \mathbf{a} \cdot \mathbf{b} \times \mathbf{c}$ is the smallest volume that fills the space by periodic repetition.
In addition to the lattice, a basis is needed to construct the crystal. The basis may be a single atom or more than one atom. The position of the atoms within the unit cell is given in fractional coordinates. Atom j is at position $\mathbf{r}_j = x_j\mathbf{a} + y_j\mathbf{b} + z_j\mathbf{c}$ with $0 \leq x_j, y_j, z_j \leq 1$.
Instead of giving the lattice in terms of the vectors **a**, **b** and **c** it can be defined using the unit cell parameters a, b, c and α, β, γ with $a = |\mathbf{a}|$, $b = |\mathbf{b}|$, $c = |\mathbf{c}|$ and $\alpha = \angle(\mathbf{b}, \mathbf{c})$, $\beta = \angle(\mathbf{a}, \mathbf{c})$, $\gamma = \angle(\mathbf{a}, \mathbf{b})$. The volume of the unit cell can then be calculated using following formula

$$V = abc\sqrt{1 - \cos^2\alpha - \cos^2\beta - \cos^2\gamma + 2\cos\alpha\cos\beta\cos\gamma} \tag{1.2}$$

This is the most general case for a triclinic unit cell, that is $a \neq b \neq c$ and $\alpha \neq \beta \neq \gamma$. For higher symmetries the formula gets simpler as some parameters are equal or angles are equal to 90°.
Planes in a crystal are determined by three points which need to be linearly independent. Planes are denoted using the Miller indices (hkl). To obtain the (hkl) values of a plane, the intersections with the unit cell axes are identified in multiples of the parameters a, b and c. The reciprocal values of these numbers are taken and multiplied to get the smallest possible integers with the same ratio. These are then the (hkl) indices of the plane or a set of parallel planes. A crystal can be represented by a set of equidistant (hkl) planes.

1.4.2 X-ray diffraction

Crystal structures can be studied by diffraction of photons, neutrons and electrons. To observe a diffraction pattern, the wavelength of the incoming waves must be of the order or smaller than the lattice constants. This is why X-rays are the preferred radiation for crystal structure analysis having wavelengths from 0.1 Å to 100 Å.

The Bragg law

The Bragg law is derived considering parallel planes of the crystal lattice and an incoming beam of X-rays. Each plane reflects a small part of the radiation with the reflected angle being equal to the incident angle. The rest is transmitted and can be reflected by the next or any of the subsequent lattice planes. The reflected beams interfere and give a diffracted beam if the interference is constructive. This occurs if the path difference is an multiple n of the incoming wavelength with n an integer. With a net plane distance of d and the incoming angle θ this gives the Bragg law.

$$n\lambda = 2d \sin\left(\frac{2\theta}{2}\right) \tag{1.3}$$

This defines the scattering angle 2θ of the diffracted beams, depending on the net plane distance d of the crystal structure. However, no information on the basis of the crystal is included.

The reciprocal lattice

The basis of the crystal determines the distribution of the electrons within the unit cell which in turn determines the relative intensity of the scattered beams. Like all physical properties within a crystal also the electron number density is invariant under a translation given by $\mathbf{R}$ (equation 1.1). In one dimension Fourier analysis of the electron number density gives

$$n(x) = \sum_p n_p \, \mathrm{e}^{i\frac{2\pi p x}{a}} \tag{1.4}$$

with p an integer and n_p the Fourier coefficients. $\frac{2\pi p}{a}$ is a point in the Fourier space or reciprocal lattice. These reciprocal lattice points are the only allowed points in the Fourier series and describe the periodicity of the crystal lattice. In one dimension, the points lie on a line. In three dimensions, a set of vectors $\mathbf{G}$ needs to be defined so that the electron number density is again invariant under a translation $\mathbf{R}$.

$$n(\mathbf{r}) = \sum_{\mathbf{G}} n_{\mathbf{G}} \, \mathrm{e}^{i\mathbf{G}\mathbf{r}} \tag{1.5}$$

The vectors $\mathbf{G}$ are reciprocal space vectors

$$\mathbf{G} = h\mathbf{a}^* + k\mathbf{b}^* + l\mathbf{c}^* \tag{1.6}$$

with $\mathbf{a}^*$, $\mathbf{b}^*$ and $\mathbf{c}^*$ primitive vectors of the reciprocal lattice.

$$\mathbf{a}^* = 2\pi \frac{\mathbf{b} \times \mathbf{c}}{\mathbf{a} \cdot \mathbf{b} \times \mathbf{c}} \qquad \mathbf{b}^* = 2\pi \frac{\mathbf{c} \times \mathbf{a}}{\mathbf{a} \cdot \mathbf{b} \times \mathbf{c}} \qquad \mathbf{c}^* = 2\pi \frac{\mathbf{a} \times \mathbf{b}}{\mathbf{a} \cdot \mathbf{b} \times \mathbf{c}} \tag{1.7}$$

Laue condition

The Laue condition says that diffraction on a crystal is only possible if the scattering vector $\mathbf{q}$ is equal to a reciprocal lattice vector $\mathbf{G}_{hkl}$. The scattering vector is the difference between the wavevector of the outgoing beam $\mathbf{k}$ and the incident beam $\mathbf{k}_0$.

$$\mathbf{k} - \mathbf{k}_0 = \mathbf{q} = \mathbf{G}_{hkl} \tag{1.8}$$

Because the scattering is elastic, $\mathbf{k}_0$ and $\mathbf{k}$ are of the same length. Due to the relations between the real and the reciprocal lattice, the scattering vector $\mathbf{q}$ must be normal to the net planes (hkl). It also follows that $|\mathbf{G}_{hkl}| = |\mathbf{q}| = \frac{2\pi}{d_{hkl}}$. Inserting this into the Bragg law gives

$$|\mathbf{q}| = q = \frac{4\pi}{\lambda} \sin\theta \tag{1.9}$$

All diffraction data within this thesis will be plotted over q since this provides a wavelength independent representation.

Structure factor

The relative intensities measured in a diffraction experiment depend on the structure factor F_{hkl} of the unit cell. The intensity of a scattered beam is proportional to the square of the structure factor $I \propto |F_{hkl}|^2$. To obtain the structure factor, the integral over the charge distribution ρ_e of the unit cell is taken

$$F = \int_{uc} \rho_e(\mathbf{r})\ \mathrm{e}^{-i\mathbf{G}_{hkl}\mathbf{r}}\ \mathrm{d}\mathbf{r} \tag{1.10}$$

The charge distribution within the unit cell is the sum over the charge distributions of the individual atoms j within the basis, which are at positions $\mathbf{r}_j = x_j\mathbf{a} + y_j\mathbf{b} + z_j\mathbf{c}$. This gives

$$F = \sum_j \int_{atom} \rho_e(\mathbf{r})\ \mathrm{e}^{-i\mathbf{G}_{hkl}(\mathbf{r}-\mathbf{r}_j)}\ \mathrm{d}\mathbf{r} = \sum_j f_j\ \mathrm{e}^{i\mathbf{G}_{hkl}\mathbf{r}_j} \tag{1.11}$$

with f_j the atomic form factor. It is a measure of how strong the atom j within the unit cell scatters the incoming wave. Inserting the reciprocal lattice vector $\mathbf{G}_{hkl}$ (equation 1.6) and $\mathbf{r}_j$ gives a very convenient form of the structure factor

$$F = \sum_j f_j\ \mathrm{e}^{2\pi i(hx_j + ky_j + lz_j)} \tag{1.12}$$

The structure factor depends on the *hkl* of the reflection, the positions of the atoms within the unit cell and the atomic form factor.

The phase problem

It is relatively easy to calculate the structure factor for a given unit cell, however in the experiment only the intensity of a diffracted beam is accessible which is proportional to $|F_{hkl}|^2 = F_{hkl}F^*_{hkl}$. The phase information is lost, which means that the information about the positions of the atoms within the unit cell is lost. This is the so-called phase problem.
There are different strategies to solve the phase problem. One is using test structures. When the unit cell and the number of molecules in it are known, an educated guess can be made about the packing in the cell. Parameters are varied until the best agreement with the measured data is achieved.

Another way to solve the phase problem is the Patterson method. $|F_{hkl}|^2$ does not depend on the absolute position of the atoms, but on the distance between the atoms.

$$|F_{hkl}|^2 = \sum_j \sum_k f_j f_k \; \mathrm{e}^{i\mathbf{G}_{hkl}(\mathbf{r}_j - \mathbf{r}_k)} \tag{1.13}$$

Performing an inverse Fourier transform and introducing a relative coordinate $\mathbf{r}_j - \mathbf{r}_k = \mathbf{u} = (u, v, w)$ gives the Patterson function [28]

$$P(u, v, w) = \frac{1}{V_{\mathrm{uc}}} \sum_{hkl} |F_{hkl}|^2 \; \mathrm{e}^{-2\pi i(hu+kv+lw)} \tag{1.14}$$

Thus, relative positions between atoms can be obtained. The peak height of the Patterson function is proportional to the product of the electron densities of the two atoms, so heavy atoms give more intense peaks. To interpret the Patterson function an initial guess of the structure is necessary. If there are no heavy atoms or atoms of similar atomic number present, the interpretation becomes very difficult, but can be solved by computer algorithms.

A third frequently used way to solve the phase problem are so-called direct methods. A large number of reflections and their intensities are necessary to determine the structure, which is given by a number of crystallographic parameters one or two magnitudes lower. Atoms are most likely to be at intersections of net planes which give high intensity hkl peaks. Statistical methods based on the formula for F_{hkl} can be applied to find the structure.

The structure shown within this thesis was calculated using molecular dynamics simulations. Beginning with a test structure, 5000 structures were calculated with the program LAMMPS [29] starting with a unit cell enlarged by 10 %. Then the cell was being shrunk to its original size, performing energy minimization to find the structure with minimal energy. The final decision for a structure was made by comparing the calculated structure factors with the experimental intensities. The final structure was optimized with density functional theory using the program CASTEP [30].

2 Experimental Techniques

2.1 Sample preparation

2.1.1 Thermal vapor deposition

Thermal vapor deposition was used to prepare the samples for this thesis. Thin films are often prepared by solution processing, however, Tyrian purple has a low solubility in organic solvents due to the strong hydrogen bonding [3]. Since thermal vapor deposition is a solvent-free technique it was chosen to prepare the samples.
A rotary pump followed by a turbomolecular pump was used to obtain the vacuum in the evaporation chamber. The pressure during evaporation was within the range of $(3–6) \times 10^{-5}$ mbar.
Figure 2.1 shows the setup which is used for the deposition. Tyrian purple is evaporated from a steel Knudsen cell which is heated by a tungsten wire. The sample holder is mounted onto the upper cap of the recipient and the substrate wafer is laid face down on a copper mask. A shutter is placed underneath the wafer to start and stop the evaporation onto the substrate. Next to the sample, there is a quartz crystal microbalance, which is water-cooled. It is used to measure the mean film thickness and the evaporation rate. As more and more mass is deposited on the quartz crystal, the resonance frequency decreases. The change in frequency can be translated into a change in mass and thus in mean film thickness on the sample. For this setup and with Tyrian purple as evaporating material of a mass density of $2.1\,\mathrm{g/cm^3}$ [10], a frequency change of 1 Hz corresponds to 0.06 nm or 16.6 Hz to 1 nm.
There is no temperature control in the chamber. The heating is only regulated by the voltage applied to the heating wire around the Knudsen cell.

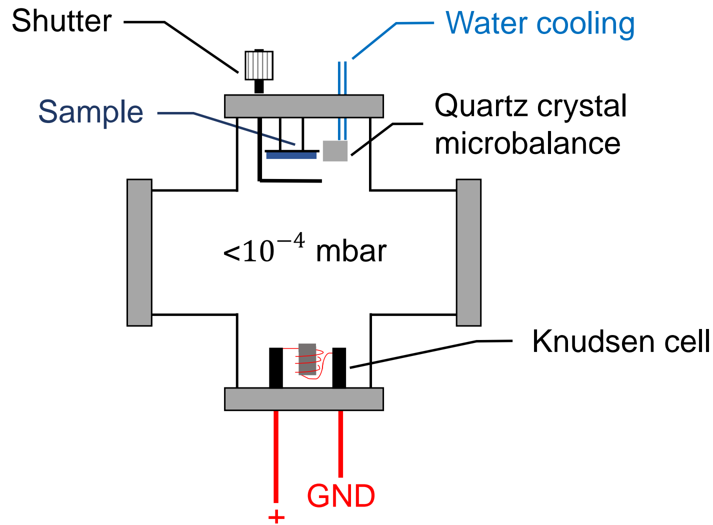

Figure 2.1: Setup used for the sample preparation by thermal vapor deposition

The evaporation rate during sample preparation was between 0.36 nm/min and 3.6 nm/min.

2.1.2 Hot wall epitaxy

Hot wall epitaxy is also a form of physical vapor deposition. The main feature is a quartz cylinder mounted between the source material and the substrate onto which the material is evaporated [31]. The cylinder can be heated so that the sample preparation happens close to thermodynamic equilibrium. The hot wall allows for a nearly uniform and isotropic flux of the source material during evaporation. The setup includes another two ovens. One heats the material which is evaporated and the other one heats the substrate, since also the substrate temperature influences the thin film growth.

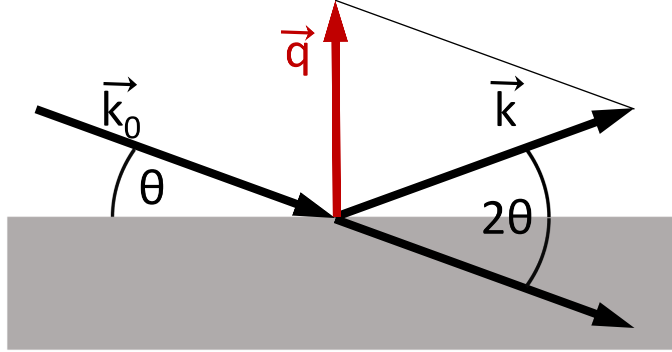

Figure 2.2: Schematic drawing of specular X-ray diffraction

2.2 X-ray diffraction

2.2.1 Specular X-ray diffraction

Specular X-ray diffraction (XRD) is an out-of-plane technique. The angles of the incident and diffracted beam are equal, which means that the lattice planes parallel to the surface are investigated [32]. The scattering vector is normal to the net planes as well as to the sample surface. Figure 2.2 shows this setup in a schematic drawing.
In a $\theta/2\theta$ scan the incidence angle θ is varied from a few degrees to some tens of degrees. The detector is always positioned at 2θ and the diffracted intensity at this angle is measured. The scattering vector $\mathbf{q}$ always stays normal to the sample surface but changes length during the measurement. The net plane distance d of planes parallel to the surface can be determined from the peak positions using the Bragg equation $d = \frac{n\lambda}{2\sin(2\theta/2)}$. The crystallite size Λ in out-of-plane direction can be determined using the Scherrer equation [33].

$$\Lambda = \frac{\lambda}{\mathrm{FWHM}\cos\left(\frac{2\theta}{2}\right)} \tag{2.1}$$

with λ the wavelength, FWHM the full width at half maximum of the peak and 2θ the scattering angle.

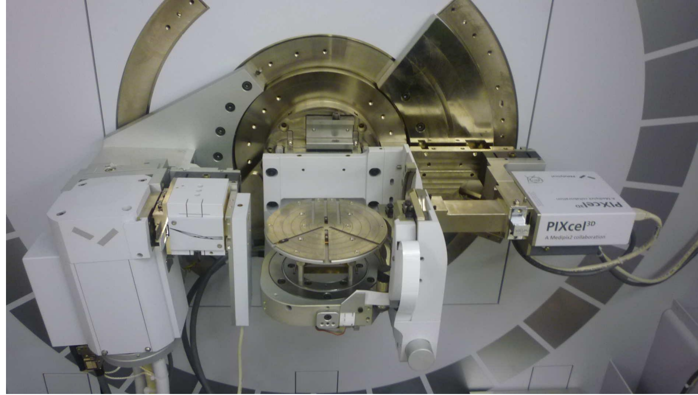

Figure 2.3: Measurement setup of the PANalytical Empyrean diffractometer. To the left is the copper tube, the sample stage in the middle and the detector to the right

The measurements were performed with a PANalytical Empyrean diffractometer. Figure 2.3 shows the experimental setup.
A copper tube is used to generate the X-rays, which is run at 40 mA and 40 kV. It is followed by the incident beam optics. It consists of a divergence slit of 1/8°, a 10 mm mask and a parallel beam mirror, which collimates the X-rays to a parallel beam and serves as monochromator so that mostly CuK_α radiation is emitted with a wavelength $\lambda = 0.154\,\text{Å}$. The incident beam also passes a beam attenuator which is programmed to insert a 0.125 mm Ni-plate above a certain count rate to protect the detector from too high intensities.
In the middle of the diffractometer there is the sample stage which is mounted on a 3-axis cradle. It can be rotated, tilted and is adjustable in height. However, during the measurement it is fixed and the tube and the detector are moved along θ and 2θ respectively.
The diffracted beam passes a 7.5 mm anti-scatter slit and a 0.02 rad Soller slit before it reaches the detector. This is a PIXcel^{3D} detector with 255x255 pixels. For XRD it is operated in 1D scanning line mode. This means that all channels are read out separately and then summed up according to the corresponding 2θ value.

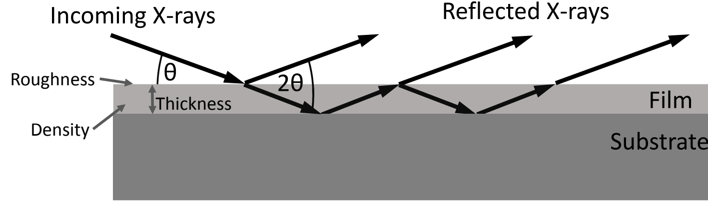

Figure 2.4: Schematic drawing of X-ray reflectivity

2.2.2 X-ray reflectivity

X-ray reflectivity (XRR) is also measured in a specular setup, that is with equal incidence and diffracted angles. However, compared to specular X-ray diffraction it is measured at very low angles from 0° to a few degrees.

X-rays have a complex index of refraction n smaller than one [34]. It is given by

$$
\begin{aligned}
n &= 1 - \delta + i\beta \\
\delta &= \frac{\lambda^2}{2\pi} r_{\mathrm{e}} \rho_{\mathrm{e}} \\
\beta &= \frac{\lambda}{4\pi} \mu_{\mathrm{x}}
\end{aligned}
\tag{2.2}
$$

with λ the wavelength, $r_{\mathrm{e}} = 2.818 \times 10^{-15}$ m the classical electron radius, ρ_{e} the electron density and μ_{x} the linear absorption coefficient.
The progression of the beam from a medium with higher index of refraction to a medium with lower index of refraction results in total external reflection when the beam hits the sample surface below a critical angle α_{C} [34].
The critical angle can be calculated using the law of Snellius, which gives

$$
\alpha_{\mathrm{C}} = \sqrt{2\delta} \tag{2.3}
$$

Above the critical angle a part of the incoming beam is reflected at the sample surface and the rest is transmitted. If this beam hits an interface to another material with a different electron density, a part is again reflected. When it again hits the surface a part of the film is reflected and a part is transmitted and so on. The diffraction geometry is shown in Figure 2.4.

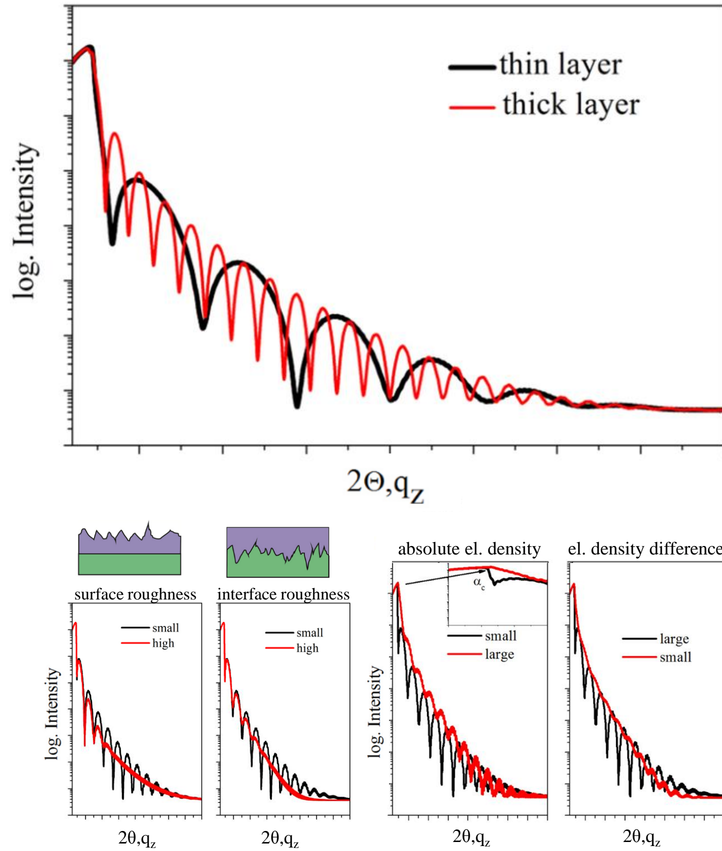

Figure 2.5: Influence of the film thickness (top), the surface and interface roughness (bottom left), and the electron density (bottom right) on X-ray reflectivity curves, figures from [27]

All waves which are reflected by the sample surface interfere, which results in an oscillating intensity as the incident angle is varied. These so-called Kiessig fringes [35] depend on the surface roughness, the interface roughness, the film thickness and electron densities of the film and the substrate. Thus, all these parameters can be obtained from the measurement. Figure 2.5 shows an overview of how these parameters influence the Kiessig fringes. The higher the film thickness, the smaller is the periodicity of the fringes. A rougher surface decreases the slope of the fringes as well as suppresses them already at lower angles than a smooth surface. For a smaller absolute electron density the fringes are much more pronounced, however, small electron density differences give hardly any fringes, since the contrast for the refracting X-rays is too low.

The parameters are calculated from fits to the measurement. Most fitting routines are based on the Parratt formalism [36]. Within this thesis two softwares are used to fit the X-ray reflectivity measurements, PANalytical X'Pert Reflectivity and Stochfit [37].
PANalytical X'Pert Reflectivity is used for fitting when there is no Bragg peak within the range in which X-ray reflectivity was measured. It fits the surface roughness and film thickness as well as the mass density of the layers. The mass density is calculated from the electron density using the chemical composition of the material. However, for measurements with a Bragg peak at a low angle PANalytical X'Pert Reflectivity is not the best option. In that case Stochfit is used. Stochfit provides a model independent fitting routine. The electron density along the surface normal is cut into thin layers. The X-ray reflectivity is then calculated for each slice. In an iterative process the electron density is varied until the calculated reflectivity curve fits the measurement. The electron density and roughness are varied during the fitting, whereas the total thickness of the film and the number of layers are input parameters and are kept constant during the calculation [37,38].

The same experimental setup was used for X-ray reflectivity measurements as for specular scans. However, a 1/32° divergence slit on the primary side and a 0.1 mm anti-scatter slit on the secondary side were used. The detector was operated in 0D receiving slit mode with three open channels.

Heating experiments

Experiments using a DHS900 heating stage were also performed using this experimental setup. The dome of the stage was flooded with helium to prevent oxidation of the film.

2.2.3 Grazing incidence X-ray diffraction

Grazing incidence X-ray diffraction (GIXD) is a surface sensitive technique which is used to analyze the in-plane structure of thin films. The incident beam hits the sample at very low angles, more precisely at angles below the

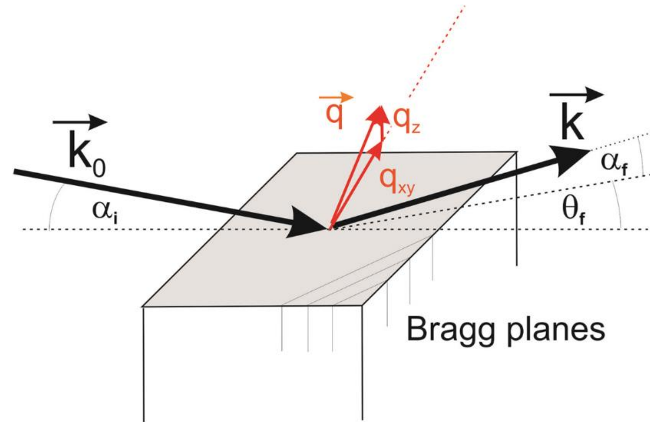

Figure 2.6: Schematic drawing of grazing incidence X-ray diffraction, figure from [27]

critical angle of the substrate, so that the X-rays do not enter the substrate. An evanescent wave is formed at the surface, which decays exponentially perpendicular to the sample surface. However, directly at the surface the wave has still oscillation character [39].

This wave diffracts from net planes which are not parallel to the substrate surface, as compared to specular X-ray diffraction where only parallel planes can be investigated. Thus, GIXD gives information about the in-plane structure of thin films. The diffraction geometry is shown in Figure 2.6.

Grazing incidence X-ray diffraction experiments were performed at the European Synchrotron Radiation Facility (ESRF), beamline ID10. A beam of 22 keV, 0.56 Å was used with a cross section of $20 \times 20\,\mu$m. The incident angle was chosen to be the one giving the highest intensity. A lead pinhole was used in front of the sample to reduce air scattering, as well as a lead beam stop, which was mounted right behind the sample to block the unscattered intensity and reduce the background. For very thin samples with low intensity, only this made it possible to measure diffraction peaks. Nitrogen was used as inert gas to reduce beam damage. Exposure times were between 10 and 30 s.

A two dimensional Pilatus detector was used to measure the diffraction patterns. These were then transformed into reciprocal space resulting in a so-called reciprocal space map. This is a cross section of the reciprocal

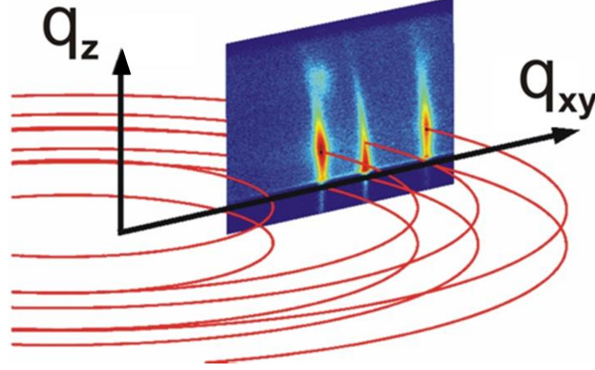

Figure 2.7: Grazing incidence X-ray diffraction is used to measure a cross section of the reciprocal space, figure from [27]

space, see Figure 2.7. The in-plane component of the scattering vector $q_{xy} = \sqrt{q_x^2 + q_y^2}$ is plotted on the x-axis and the out-of-plane coordinate q_z of the scattering vector is plotted on the y-axis. Each peak in the map results from diffraction at specific net planes in the crystal. The maps were indexed with unit cells using the in-house software PyGid. This is a trial-and-error method. The unit cell parameters are varied until the calculated diffraction pattern fits onto the measurement.
Some samples were also indexed using analytical calculations based on the following equations

$$\begin{aligned} \begin{pmatrix} q_{xy1}^2 \\ q_{xy2}^2 \\ q_{xy3}^2 \end{pmatrix} &= \begin{pmatrix} h_1^2 & k_1^2 & -2h_1k_1 \\ h_2^2 & k_2^2 & -2h_2k_2 \\ h_3^2 & k_3^2 & -2h_3k_3 \end{pmatrix} \begin{pmatrix} \left(\frac{2\pi}{a\sin\gamma}\right)^2 \\ \left(\frac{2\pi}{b\sin\gamma}\right)^2 \\ \frac{2\pi}{a\sin\gamma}\frac{2\pi}{b\sin\gamma}\cos\gamma \end{pmatrix} \\ \begin{pmatrix} q_{z1} \\ q_{z2} \\ q_{z3} \end{pmatrix} &= \begin{pmatrix} -h_1 & -k_1 & l_1 \\ -h_2 & -k_2 & l_2 \\ -h_3 & -k_3 & l_3 \end{pmatrix} \begin{pmatrix} \frac{2\pi}{a\sin\gamma}\ \delta \\ \frac{2\pi}{b\sin\gamma}\ \mu \\ \frac{2\pi}{c\sin\epsilon} \end{pmatrix} \end{aligned} \tag{2.4}$$

with

$$\begin{aligned} \delta = \frac{\cos\beta - \cos\alpha\cos\gamma}{\sin\gamma\sin\epsilon}, \quad \mu = \frac{\cos\alpha - \cos\beta\cos\gamma}{\sin\gamma\sin\epsilon} \\ \sin\epsilon = \frac{c_z}{c} = \frac{\sin\gamma}{\sqrt{\sin^2\gamma + \delta^2 + \mu^2 + 2\delta\mu\cos\gamma}} \end{aligned} \tag{2.5}$$

These are derived from geometrical considerations and are valid for triclinic unit cells with contact plane (001) to the substrate, that is with basis vectors **a** and **b** lying on the substrate. Knowing three peak positions and their corresponding *hkl* values, all six unit cell parameters can be calculated, under the condition that the *hkl* are linearly independent.

3 Substrates and Samples

3.1 Substrate preparation

3.1.1 Silicon oxide substrates

Samples were prepared on silicon wafers with a 150 nm thermal oxide grown on top. Two different cleaning routines were used to prepare the substrates for the sample evaporation.
Firstly, silicon wafers were put in acetone in an ultrasonic bath for 10 min, which was also heated. Then they were rinsed with isopropanol and let to dry. Wafers which were prepared in this way will be further called conventionally cleaned silicon oxide or just silicon oxide.
Secondly, substrates were also cleaned by plasma etching. A Femto plasma cleaner by Diener electronic was used. Oxygen plasma was ignited for 42 s to clean the wafers.

3.1.2 Polymer substrates

In addition to the bare silicon oxide substrates, also substrates with a polymer film on top were used. These have different roughnesses, thicknesses and surface energies. The polymers used were ethylene glycol dimethacrylate (EGDMA), hexamethyldisiloxane (HMDSO) and 1H,1H,2H,2H-perfluorodecyl acrylate (PFDA). Their chemical structures are shown in Figure 3.1. The polymer substrates were prepared by chemical vapor deposition (CVD). EGDMA and PFDA were prepared by initiated chemical vapor deposition (iCVD). iCVD is a free-radical polymerization method [40]. Initiator and monomer molecules are introduced into a vacuum chamber in the gas phase. The initiator molecules are decomposed by heating filaments, thus produc-

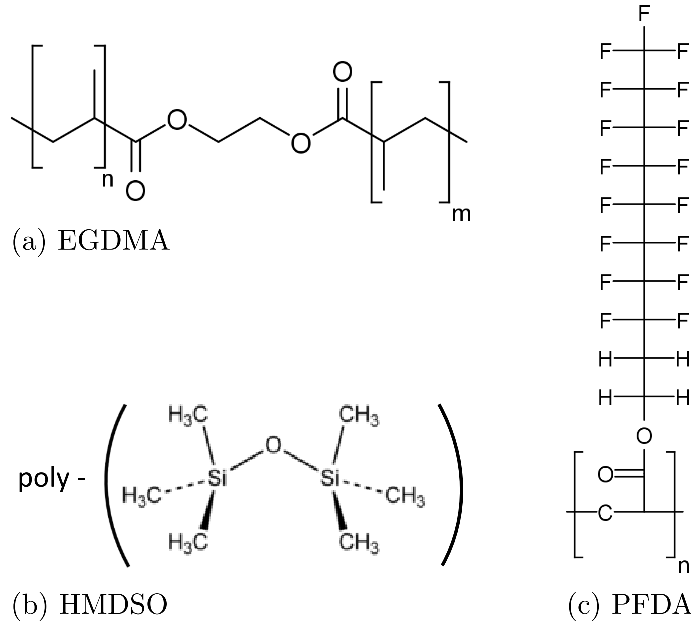

(a) EGDMA

(b) HMDSO

(c) PFDA

Figure 3.1: Chemical structures of (a) ethylene glycol dimethacrylate (EGDMA), (b) hexamethyldisiloxane (HMDSO) and (c) 1H,1H,2H,2H-perfluorodecyl acrylate (PFDA)

ing free radicals. The radicals and the monomer units reach the substrate where they react and chain polymerization follows. The polymerization terminates when two radicals react [41,42].

HMDSO substrates were prepared by plasma enhanced chemical vapor deposition (PECVD). In PECVD the monomer units are introduced into the reactor in the gas phase. A plasma is ignited which excites, ionizes or fragments the monomer molecules. Radicals are produced by dissociation of molecules. These can be further fragmented or react with other radicals or molecules, forming polymers. Electrons in the plasma can activate the polymers already absorbed at the surface, creating free bonds allowing further polymerization [41,43].

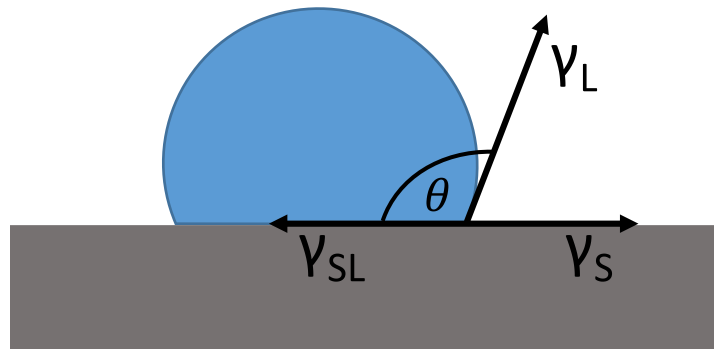

Figure 3.2: Schema of a contact angle measurement.
γ_{S} ... surface energy
γ_{L} ... surface tension of the liquid
γ_{SL} ... interfacial tension between liquid and solid
θ ... contact angle

3.2 Substrate characterization

3.2.1 Contact angle measurements

Contact angle measurements were performed on the different substrates to determine their surface energy. The surface energy is the energy needed to take a molecule from the bulk to the surface, which is an unfavorable state due to missing bonds to neighboring molecules.
The relationship between the surface energy and the contact angle for a liquid drop on the surface is given by Young's equation [44].

$$\gamma_{\mathrm{S}} = \gamma_{\mathrm{L}} \cos\theta + \gamma_{\mathrm{SL}} \tag{3.1}$$

γ_{S} is the surface energy, γ_{L} the surface tension of the liquid, θ the contact angle and γ_{SL} the interfacial tension between the liquid and the solid [44]. This is shown in Figure 3.2.
Only θ and γ_{L} can be measured. To obtain γ_{S} there are different approaches, mainly the method of Zisman [45] and the method of Owens and Wendt [44], the latter being used within this work.

According to Fowkes [46], the surface energy can be separated depending on the origin of the contributions to the surface energy.

$$\gamma = \gamma^{\mathrm{d}} + \gamma^{\mathrm{h}} \tag{3.2}$$

γ^{d} is the contribution due to the dispersive forces and γ^{h} is the polar part which mainly arises due to hydrogen bonding. Inserting the ansatz for γ_{SL}

$$\gamma_{\mathrm{SL}} = \gamma_{\mathrm{S}} + \gamma_{\mathrm{L}} - 2\sqrt{\gamma_{\mathrm{S}}^{\mathrm{d}}\gamma_{\mathrm{L}}^{\mathrm{d}}} - 2\sqrt{\gamma_{\mathrm{S}}^{\mathrm{h}}\gamma_{\mathrm{L}}^{\mathrm{h}}} \tag{3.3}$$

into Young's equation gives

$$1 + \cos\theta = 2\sqrt{\gamma_{\mathrm{S}}^{\mathrm{d}}}\frac{\sqrt{\gamma_{\mathrm{L}}^{\mathrm{d}}}}{\gamma_{\mathrm{L}}} + 2\sqrt{\gamma_{\mathrm{S}}^{\mathrm{h}}}\frac{\sqrt{\gamma_{\mathrm{L}}^{\mathrm{h}}}}{\gamma_{\mathrm{L}}} \tag{3.4}$$

Measuring the contact angle θ for two liquids with known $\gamma_{\mathrm{L}}^{\mathrm{d}}$ and $\gamma_{\mathrm{L}}^{\mathrm{h}}$ allows to calculate $\gamma_{\mathrm{S}}^{\mathrm{d}}$ and $\gamma_{\mathrm{S}}^{\mathrm{h}}$. This was done for all substrates using water and diiodomethane as liquids.

3.2.2 Atomic force microscopy

Atomic force microscopy (AFM) is a measurement method to investigate the morphology of surfaces with a very high resolution down to a nanometer scale [47]. Its main component is a microfabricated cantilever with a very sharp tip, which probes the sample surface. It is scanned over the sample while interacting with the surface. In tapping mode it is oscillating and the amplitude is measured. Due to van der Waals forces, dipole-dipole forces and electrostatic forces, the amplitude decreases as the tip gets close to the surface. The change in amplitude is measured using a laser. A feedback system is implemented to keep the cantilever at constant height above the sample, which is used to measure the topography of the sample.
Attempts were made to measure Tyrian purple by AFM, but unfortunately, it was not possible to get good results. That is why only the polymer substrates were characterized by AFM.

3.3 Polymer substrates

3.3.1 EGDMA (Ethylene glycol dimethacrylate)

X-ray reflectivity was measured on the EGDMA substrate. The measured data is shown in Figure 3.3 in blue and the fit in red. PANalytical X'Pert Reflectivity was used to calculate the fit. The obtained parameters are the density $\rho = 1.23\,\mathrm{kg/cm^3}$, the thickness of the EGDMA polymer layer $d = 16.6\,\mathrm{nm}$, and the roughness $\sigma_{\mathrm{XRR}} = 1.16\,\mathrm{nm}$.
Figure 3.4 shows an AFM image of the substrate. The roughness extracted from this measurement is $\sigma_{\mathrm{AFM}} = 1.07\,\mathrm{nm}$ which compares quite well to the roughness obtained by XRR.

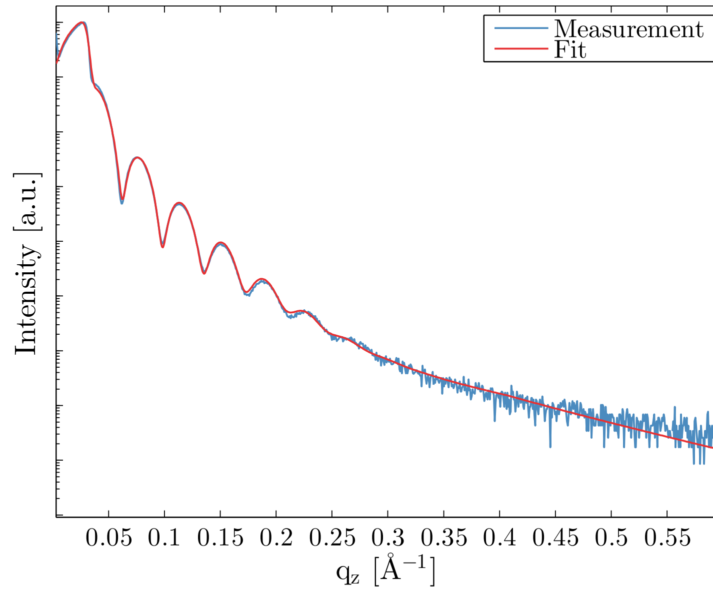

Figure 3.3: X-ray reflectivity measurement of the EGDMA substrate. Comparison of measured data and the corresponding fit

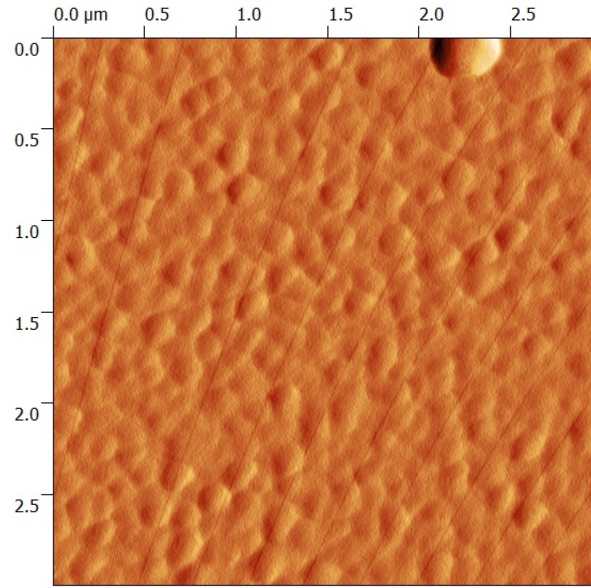

Figure 3.4: Atomic force microscopy image of the EGDMA substrate surface

3.3.2 HMDSO (Hexamethyldisiloxane)

X-ray reflectivity was also measured on the HMDSO substrate. The measurement and the fit are shown in Figure 3.5. In this measurement two critical angles can be distinguished. They are $\alpha_C = 0.16°$ and $\alpha_C = 0.21°$, the former being the one of the HMDSO film and the latter of silicon oxide [48]. From the critical angle of HMDSO the electron density can be calculated using equations 2.2 and 2.3. It has a value of $367\,\mathrm{nm}^{-3}$. The parameters extracted from the fit are the density $\rho = 0.92\,\mathrm{kg\,cm}^{-3}$, the thickness of the polymer layer $d = 70.0\,\mathrm{nm}$, and the roughness $\sigma_{\mathrm{XRR}} = 0.66\,\mathrm{nm}$.
AFM was measured for the HMDSO substrate. It is shown in Figure 3.6. The roughness obtained from this measurement is $\sigma_{\mathrm{AFM}} = 0.70\,\mathrm{nm}$, which is comparable to the roughness σ_{XRR}.

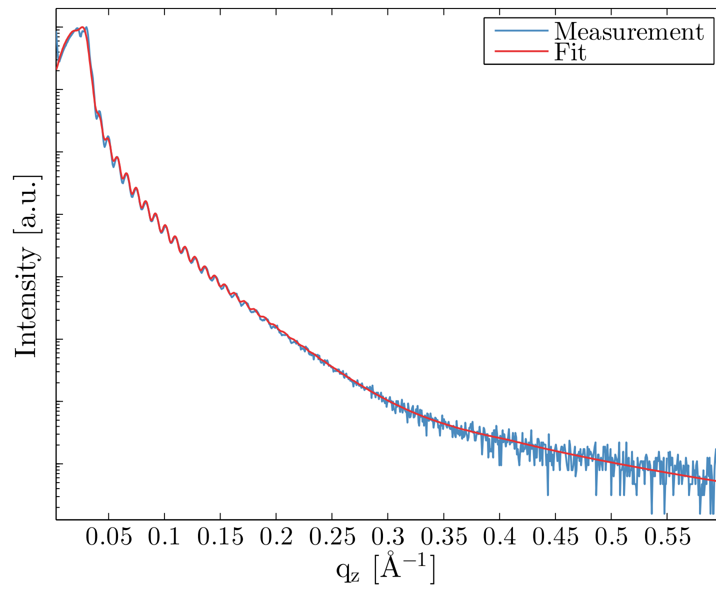

Figure 3.5: X-ray reflectivity measurement of the HMDSO substrate. Comparison of measured data and the corresponding fit

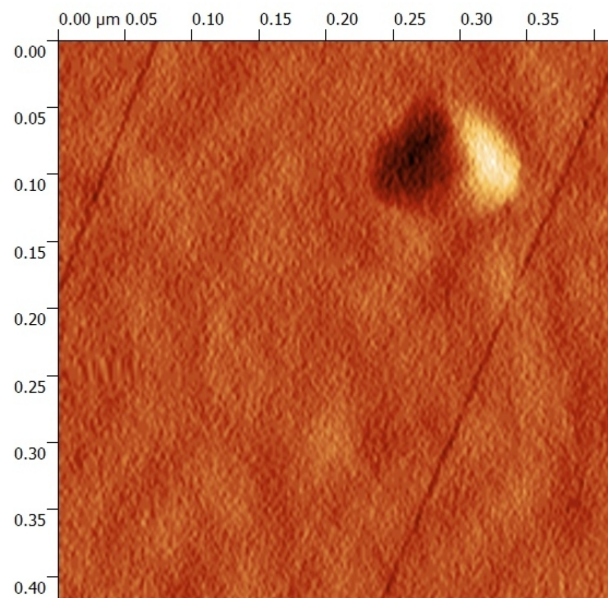

Figure 3.6: Atomic force microscopy image of the HMDSO substrate surface

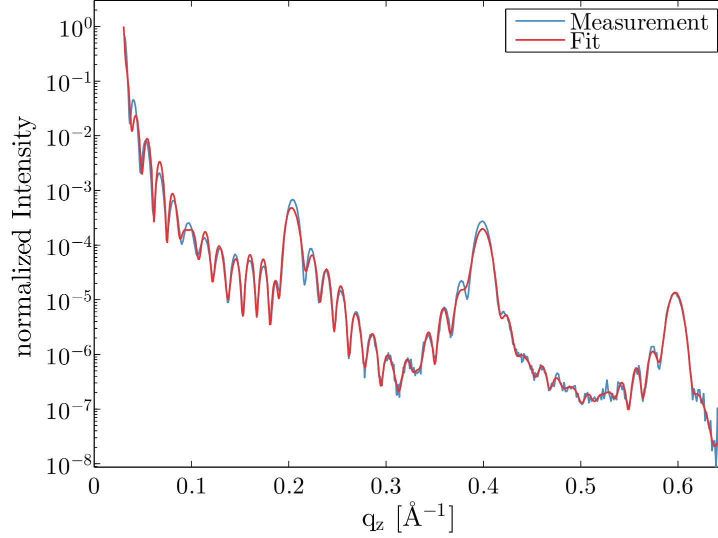

Figure 3.7: X-ray reflectivity measurement (blue) and fit (red) of the PFDA substrate

3.3.3 PFDA (1H,1H,2H,2H-perfluorodecyl acrylate)

The PFDA substrate was also characterized using X-ray reflectivity, which is shown in Figure 3.7. The measurement shows Bragg peaks together with Kiessig fringes. This is because PFDA prepared by iCVD forms crystalline domains, in the particular case with a preferred orientation [49]. It aggregates in a smectic B phase with a bilayer structure of 32.4 Å periodicity. The red curve in Figure 3.7 is the fit which was calculated using the software Stochfit [37] (see section 2.2.2). Data were cut off before the critical angle to make the calculation run faster. Figure 3.8 shows the corresponding electron density in direction normal to the surface. The coordinate z starts at the interface of the polymer layer and the underlying substrate wafer and points outwards throughout the PFDA layer. The electron density shows periodic spikes in the middle of the layer from about 15 to 40 nm. Their periodicity is (3.1 ± 0.1) nm, which corresponds well to the known bilayer distance of 3.24 nm [49]. The parameters used to obtain the fit were a thickness of 50 nm and 500 boxes. The electron density drops abruptly at 50 nm, that is at the PFDA/air interface, which shows that the PFDA layer is relatively smooth. Figure 3.9 shows an AFM measurement of the PFDA surface. The roughness obtained is $\sigma_{\mathrm{AFM}} = 3.62$ nm.

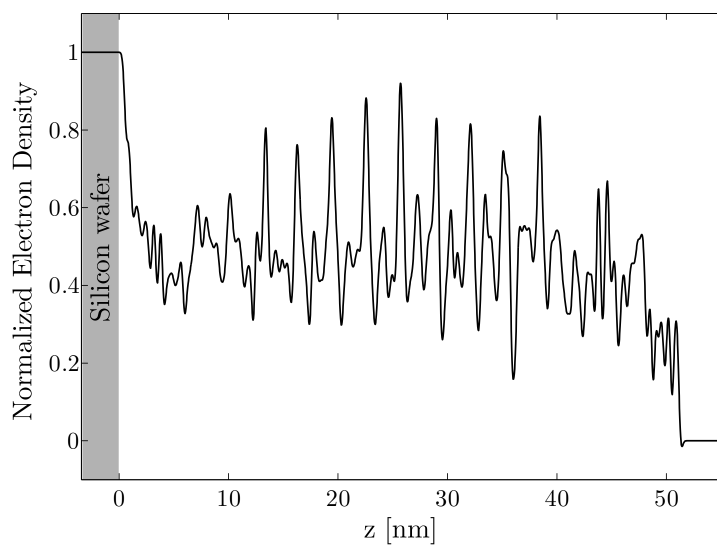

Figure 3.8: Normalized electron density parallel to the surface normal calculated with Stochfit for the PFDA substrate

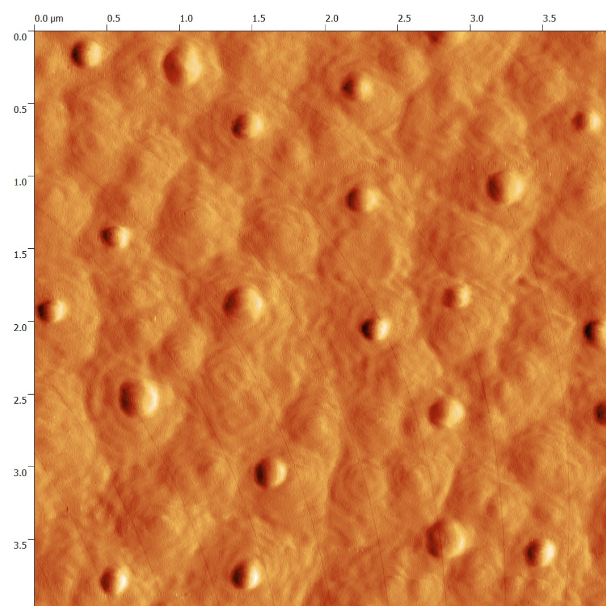

Figure 3.9: Atomic force microscopy image of the PFDA substrate surface

3.4 Surface energies of the substrates

On the two differently cleaned silicon oxide substrates, as well as on the polymer substrates, contact angle measurements were performed. Water and diiodomethane were used as liquids. Their contact angles were used to calculate the dispersive and polar part of the surface energy, which give the total surface energy. Table 3.1 shows the results in decreasing order of the surface energy. It also gives the dispersive and polar part separately, as well as the contact angles. The plasma etched SiO_2 substrate has the highest surface energy as well as the highest polar part. The conventionally cleaned SiO_2 has a somewhat lower surface energy and polar part, whereas the dispersive part is nearly the same. This shows that plasma etching enhances the hydrophilicity of the SiO_2 surface. During the plasma etching process the carbon surface contaminations are replaced by hydroxyl groups and dangling bonds [50,51]. The polymer substrates have smaller surface energies and higher water contact angles than both SiO_2 substrates. In particular, PFDA has the smallest polar part, resulting in a high water contact angle of nearly 120°. This is due to the fluorinated chains of the PFDA molecules (see Figure 3.1c).

Table 3.1: Contact angle measurements of the substrates: Surface energies and water contact angle
γ [mN/m] ... total surface energy
γ^{d} [mN/m] ... dispersive part of the surface energy
γ^{h} [mN/m] ... polar part of the surface energy
θ_{W} [°] ... contact angle of water
θ_{I} [°] ... contact angle of diiodomethane

	γ [mN/m]	γ^{d} [mN/m]	γ^{h} [mN/m]	θ_{W} [°]	θ_{I} [°]
SiO_2, plasma etched	73.4±0.1	38.5±0.1	34.9±0.1	17.3±0.2	42.2±0.1
SiO_2	61.3±0.1	37.4±0.1	23.9±0.1	42.6±0.1	44.2±0.9
EGDMA	43.2±0.1	31.2±0.1	12.1±0.1	66.6±0.5	55.5±0.3
HMDSO	25.0±0.2	19.1±0.1	5.9±0.1	87.8±0.9	76.8±0.7
PFDA	12.4±0.3	12.3±0.3	0.1±0.1	119.6±0.5	90.9±0.9

3.5 Sample overview

Table 3.2 gives an overview of the samples which were prepared and measured within this work.

Table 3.2: Overview of the Tyrian purple samples prepared and analyzed within this thesis
Δf [Hz] ... frequency change of the quartz microbalance during evaporation
d [nm] ... nominal thickness

Substrate	Δf [Hz]	d [nm]
SiO_2	10	0.6
	15	0.9
	25	1.5
	50	3.0
	75	4.5
	100	6.0
	150	9.0
	150	9.0
plasma etched SiO_2	10	0.6
	15	0.9
	25	1.5
	50	3.0
	75	4.5
	100	6.0
	150	9.0
EGDMA	792	47.5
	162	9.7
	106	6.4
HMDSO	306	18.4
	150	9
PFDA	150	9

4 Results and Discussion

4.1 Bulk phase and surface induced phase

Samples were prepared by hot wall epitaxy on different substrates and at different substrate temperatures. Figure 4.1 shows specular X-ray diffraction measurements for Tyrian purple prepared on a polyethylene substrate. The *hkl* indices correspond to the known peaks of the crystal bulk phase (see section 1.1.3). The arrows point to peaks which are expected to be from the surface induced phase. On the sample evaporated on polyethylene at 50 °C only these peaks are visible, whereas at higher temperatures the bulk peaks increase compared to the peaks of the surface induced phase.

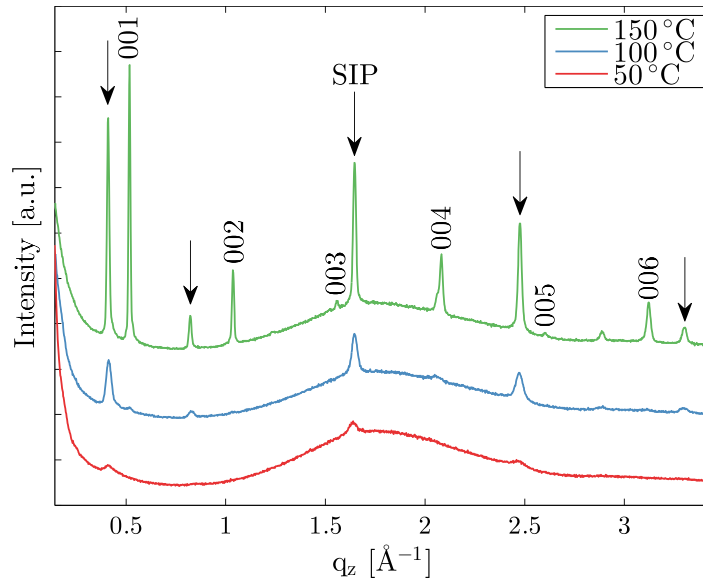

Figure 4.1: Specular X-ray diffraction - Tyrian purple on polyethylene prepared by hot wall epitaxy at substrate temperatures 50 °C, 100 °C and 150 °C. The *hkl* values denote peaks of the bulk phase and the arrows indicate peaks of the surface induced phase (SIP).

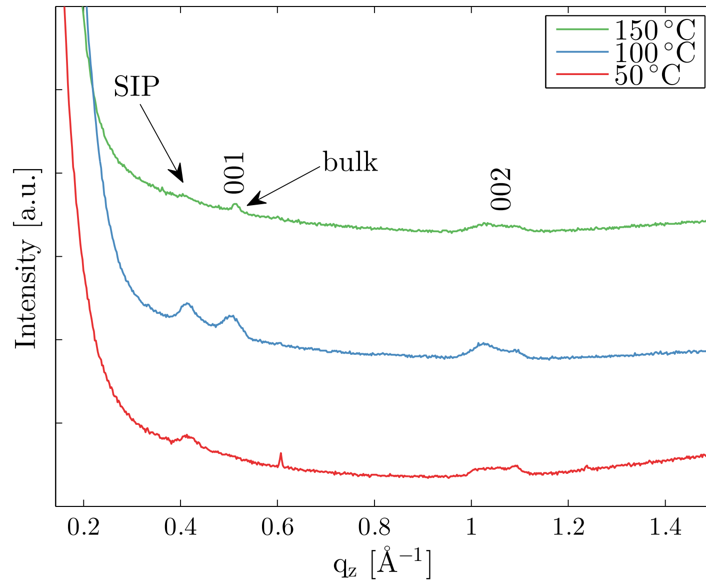

Figure 4.2: Specular X-ray diffraction - Tyrian purple on silicon oxide prepared by hot wall epitaxy at substrate temperatures 50 °C, 100 °C and 150 °C.

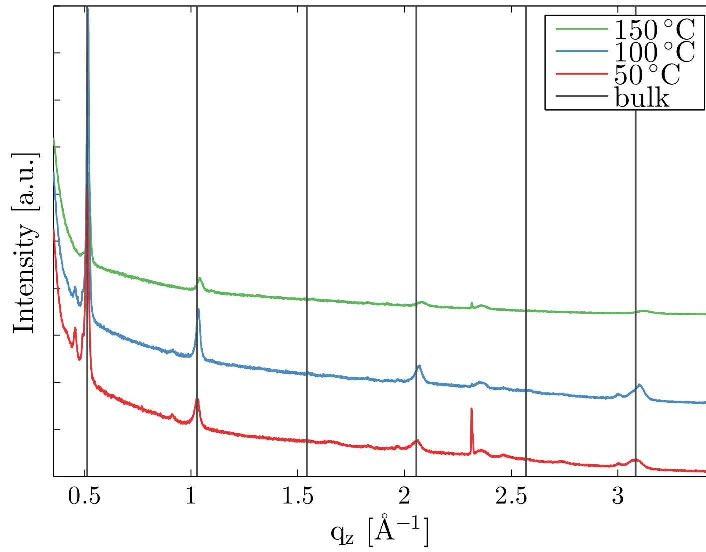

Figure 4.3: Specular X-ray diffraction - another set of samples: Tyrian purple on silicon oxide, prepared by hot wall epitaxy at substrate temperatures 50 °C, 100 °C and 150 °C. The vertical lines indicate the Bragg peaks of the crystal bulk phase.

The same tendency is visible on a silicon oxide substrate (Figure 4.2), especially for the first peak. For 50 °C, only the peak associated with the surface induced phase is observed. For 100 °C, both peaks have approximately the same intensity and on the 150 °C substrate the bulk peak is dominant.
The sample preparation was repeated on silicon oxide substrates, and these show the same structural features as the previous samples. The sample at 150 °C shows only the bulk phase. The measurement is shown in Figure 4.3.

Grazing incidence X-ray diffraction

Figure 4.4 shows an example of a reciprocal space map measured with GIXD for the 100 °C sample shown in Figure 4.2. The black indices belong to the crystal bulk phase given in Table 1.1 [9] with a contact plane (100) to the substrate. Only peaks with an observable intensity are indexed. Some additional peaks are indexed in white. These belong to the surface induced phase. The unit cell parameters are $a = 3.85\,\text{Å}$, $b = 5.84\,\text{Å}$, $c = 15.22\,\text{Å}$, $\alpha = 94.4°$, $\beta = 94.4°$, $\gamma = 86.7°$, $V = 340.22\,\text{Å}^3$.
For a 150 °C sample, only bulk peaks are measured with GIXD (Figure 4.5), which is in accordance with the specular X-ray measurements. The incident angles for grazing incidence diffraction were always chosen to be the ones giving the highest intensity. For the 100 °C sample this was $\alpha_\text{i} = 0.08°$ and for the 150 °C sample $\alpha_\text{i} = 0.065°$.

To sum up, the higher the substrate temperature during the sample preparation, the more likely the bulk phase appears. Since the aim of this work was to investigate the surface induced crystal phase, further sample preparation was performed with substrates held at room temperature during the evaporation.

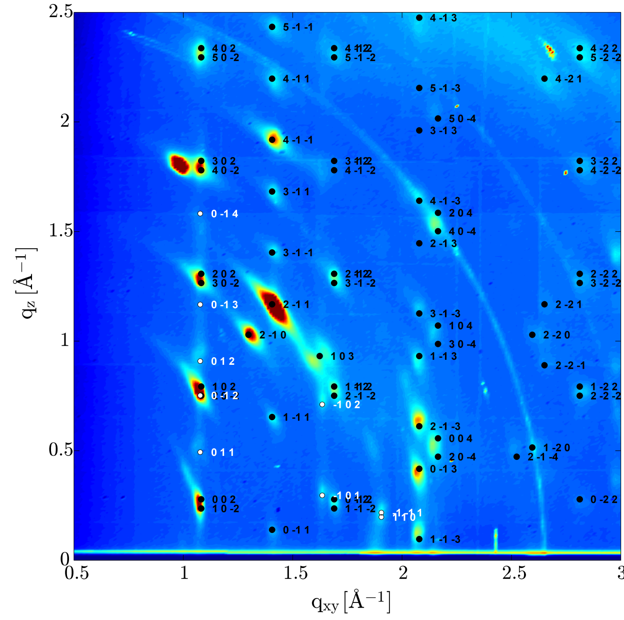

Figure 4.4: Reciprocal space map: Tyrian purple on SiO_2, 100 °C sample from Figure 4.2. Black indices belong to the bulk phase (Table 1.1, [9]), the white indices belong to the surface induced phase with parameters $a = 3.85$ Å, $b = 5.84$ Å, $c = 15.22$ Å, $\alpha = 94.4°$, $\beta = 94.4°$, $\gamma = 86.7°$.

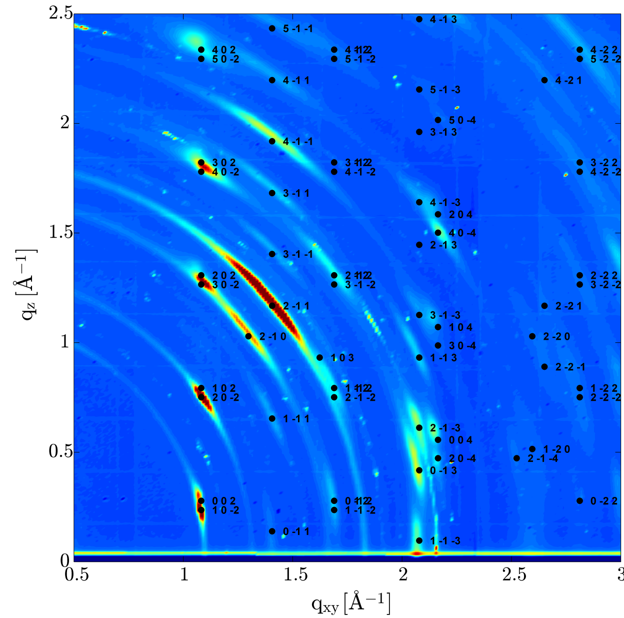

Figure 4.5: Reciprocal space map: Tyrian purple on SiO_2, 150 °C sample from Figure 4.3. The indexation represents the diffraction peaks of the crystal bulk phase (Table 1.1, [9])

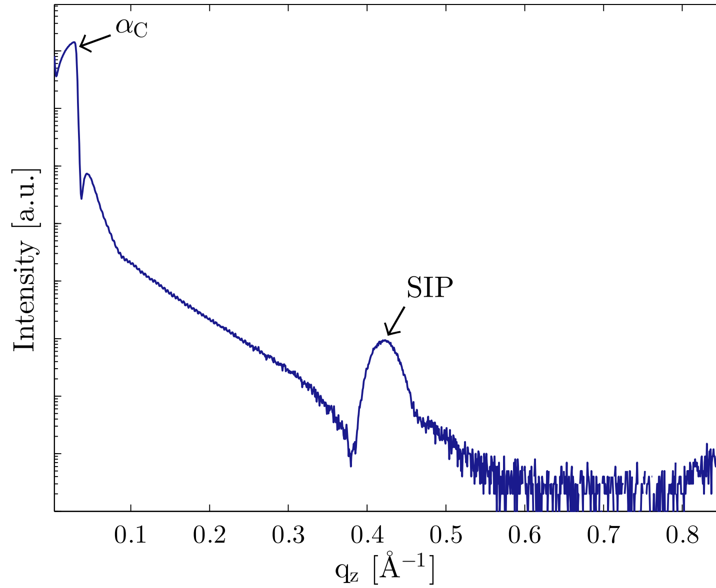

Figure 4.6: X-ray reflectivity of a sample prepared on conventionally cleaned SiO_2 with 9 nm nominal thickness

4.2 Surface induced phase on SiO_2

4.2.1 On conventionally cleaned SiO_2

Samples were prepared on conventionally cleaned SiO_2 by thermal evaporation. Figure 4.6 shows the X-ray reflectivity curve of a sample with 9 nm nominal thickness.

The main features of this measurement are the critical angle α_C, one Kiessig fringe, and the Bragg peaks at $q_z = 0.41\,\text{Å}^{-1}$ and $q_z = 0.83\,\text{Å}^{-1}$. The critical angle is at $0.029\,\text{Å}^{-1}$ corresponding to an incident angle $\alpha_i = 0.21°$. Just one critical angle is visible because the electron density of the SiO_2 substrate and the Tyrian purple film are comparable. They are $\rho_e = 670\,\text{nm}^{-3}$ for SiO_2 [48] and $\rho_e = 601\,\text{nm}^{-3}$ for Tyrian purple calculated based on the crystal structure of the bulk phase [10]. These give calculated critical angles of $\alpha_{C,SiO_2} = 0.216°$ and $\alpha_{C,TP} = 0.205°$ respectively, which are difficult to distinguish experimentally. The small difference in electron densities might also be the reason why there is only one pronounced Kiessig fringe.

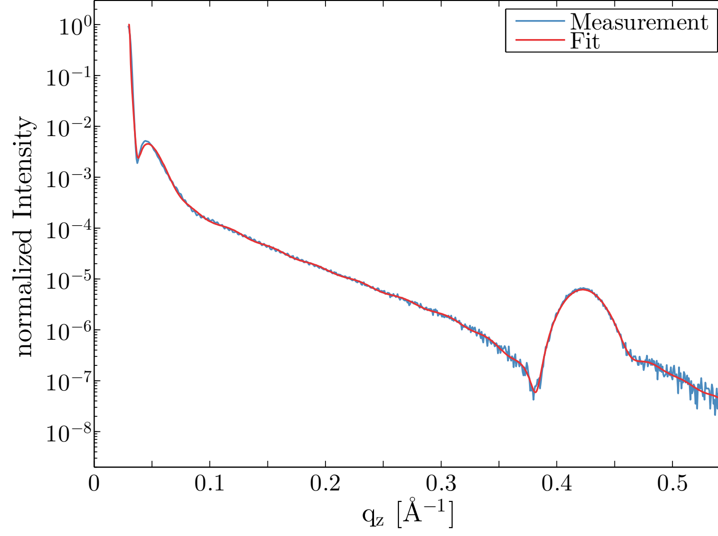

Figure 4.7: X-ray reflectivity - Comparison of measured and fitted data for a sample on conventionally cleaned SiO_2 with a 9 nm nominal thickness

The position of the Bragg peak at $q_z = 0.41\,\text{Å}^{-1}$ ($2\theta = 5.87°$) does not correspond to the 100 peak of the bulk phase which would be expected at $q_z = 0.51\,\text{Å}^{-1}$ ($2\theta = 7.23°$), but to the surface induced structure which was already presented in Figures 4.1 and 4.2. This means that the approach to evaporate a thin film of Tyrian Purple onto a substrate at room temperature indeed results in the surface induced crystal phase.
Since there is only one Kiessig fringe, the determination of the sample thickness proved difficult. The software Stochfit [37] was used to fit the measured data.
Figure 4.7 compares the fit with the measurement. Again, data were cut off before the critical angle and after the Bragg peak. As can be seen, the agreement between the measured data and the calculated fit is very good.
The calculated electron density in direction normal to the film-substrate interface is shown in Figure 4.8. z is the out-of-plane coordinate pointing perpendicular from the substrate with the interface at $z = 0$ nm. Right above the interface, the electron density decreases sharply to a minimum. Then the electron density profile is periodic with a periodicity of $d = (1.5 \pm 0.2)$ nm, which corresponds to the long molecular axis of Tyrian purple. While the periodicity must be correct in order to reproduce the Bragg peak, the be-

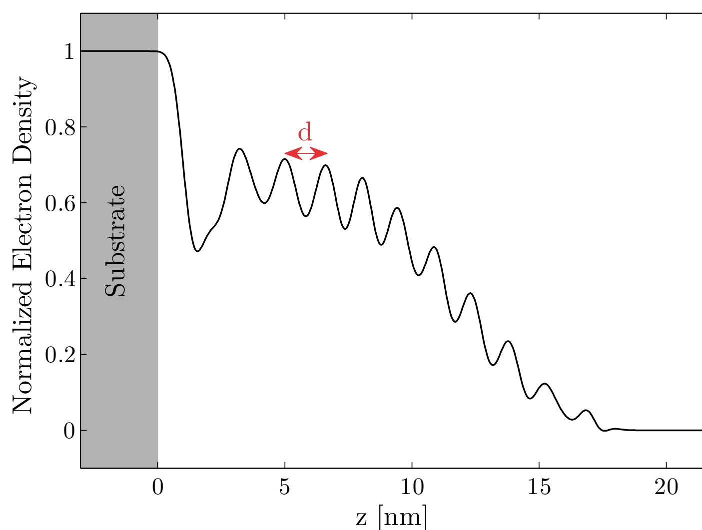

Figure 4.8: Normalized electron density calculated with Stochfit for a sample on conventionally cleaned SiO_2 with a 9 nm nominal thickness

havior of the curve between the maxima and minima might not reflect the real electron density. Considering the chemical structure of Tyrian purple (Figure 1.1), the electron density profile is not sinusoidal. It has a maximum where two bromine atoms of two molecules meet and a minimum at the double bond at the center of the molecule.
After about five maxima, the electron density smears out. This suggests that there are islands of standing molecules on the substrate. Therefore, the film thicknesses given are always nominal thicknesses calculated from the change in frequency of the quartz microbalance during evaporation (see section 2.1.1) and thus average thicknesses of the film and not the maximal thickness. The thickness which was given as input parameter for the fit was 16 nm. This is considerably more than the 9 nm nominal thickness and accounts for the formation of islands. 120 boxes were used to perform the calculation.

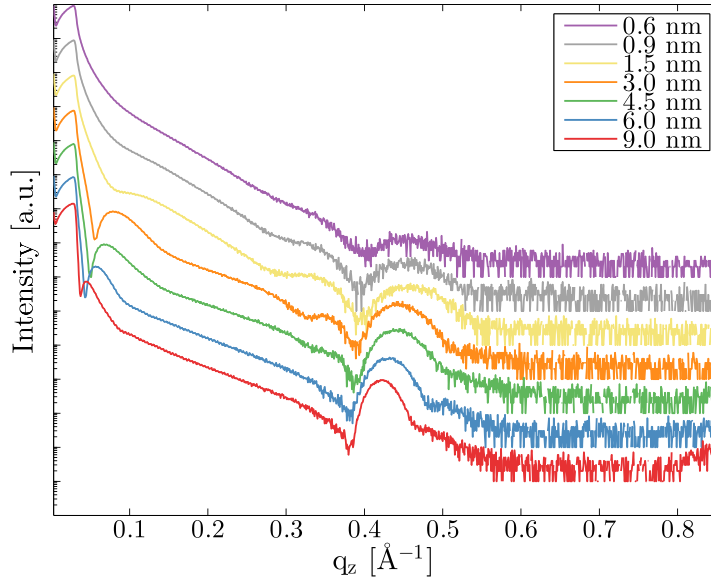

Figure 4.9: X-ray reflectivity for a series of samples with different film thicknesses on conventionally cleaned SiO_2

Samples of different thicknesses

Samples of thicknesses between 0.6 nm and 9 nm were prepared. All XRR measurements are depicted in Figure 4.9.

With decreasing film thickness, the Bragg peak broadens but it never disappears completely, even for the thinnest sample. For Tyrian purple, a frequency change of 25 Hz of the quartz microbalance would correspond to 1.5 nm which is a monolayer of standing molecules. However, also samples of 0.9 nm and 0.6 nm nominal thickness show a Bragg peak which means that there is some formation of crystallites out-of-plane. Therefore, there cannot be a monolayer on any of the samples. Rather island growth is suggested again, which was also observed for indigo [52]. The molecules within an island are more strongly bound to each other than to the substrate. A schematic of molecules oriented perpendicular to the substrate surface is drawn in Figure 4.10.

The peak broadening is related to the crystallite size. The sharper a peak the larger the crystallite and the broader the peak, the smaller the crystallite. The crystallite size can be calculated via the Scherrer formula (equation 2.1). The results are given in Table 4.1. Instrumental errors were not con-

Table 4.1: X-ray reflectivity for different film thicknesses on SiO_2: peak positions and estimates of crystallite size
2θ [°] ... position of Bragg peak
q_z [Å^{-1}] ... position of Bragg peak in reciprocal space
FWHM [°] ... full width at half maximum of Bragg peak
Λ [Å] ... estimate of crystallite size, calculated with equation 2.1
q_{α_C} [Å^{-1}] ... position of the critical angle in reciprocal space
α_C [°] ... critical angle

Sample	2θ [°]	q_z [Å^{-1}]	FWHM [°]	Λ [Å]	q_{α_C} [Å^{-1}]	α_C [°]
0.6 nm	6.40	0.456			0.02884	0.203
0.9 nm	6.39	0.455	1.00	83	0.02884	0.203
1.5 nm	6.45	0.460	1.05	79	0.02884	0.203
3 nm	6.29	0.448	0.72	115	0.02813	0.198
4.5 nm	6.16	0.438	0.73	114	0.02813	0.198
6 nm	6.06	0.431	0.60	137	0.02742	0.193
9 nm	5.93	0.422	0.48	171	0.02884	0.203

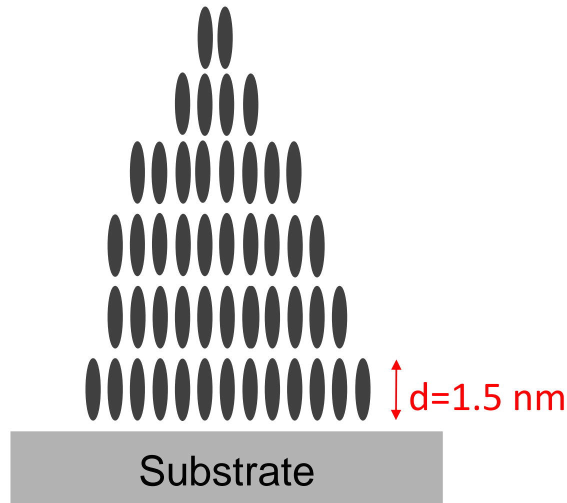

Figure 4.10: Schematic of standing molecules on a substrate, building an island. The long molecular axis is 1.5 nm.

sidered, so this gives only a rough estimate. Nevertheless, for the sample of 9 nm nominal thickness, the crystallite size of 17.1 nm corresponds to the thickness of 16 nm taken from the fit.
The critical angle lies between $q_{\alpha_C} = 0.02742\,\text{Å}^{-1}$, $\alpha_C = 0.193°$ and $q_{\alpha_C} = 0.02884\,\text{Å}^{-1}$, $\alpha_C = 0.203°$ and is also given in Table 4.1 for the individual samples. The critical angles for the samples are within a range of three measurement points, whereas the shift in positions of the Bragg peaks is more pronounced. Starting from the thickest sample the peak first shifts to the right, indicating that the net plane distance is getting smaller as the film thickness decreases. However, for the very thin samples of 0.9 nm and 0.6 nm the peak shifts to the left, which means that the net plane distance is increasing again.

Specular X-ray diffraction

Specular X-ray diffraction was measured on two samples with a 9 nm and one with a 3 nm film. The measurements are shown in Figure 4.11. All three samples have the same phase with the two thicker samples having more intensity. The vertical lines correspond to the positions of the Bragg peak of the surface induced phase. The peaks all belong to the *00l* series with the 003 peak missing.
The peak positions are given in Table 4.2. The net plane distance d_{001} was

Table 4.2: Bragg peaks of the surface induced crystal phase of Tyrian purple on SiO_2 (9 nm sample)
2θ [°] ... position of Bragg peak
q_z [Å^{-1}] ... position of Bragg peak in reciprocal space
d_{001} ... net plane distance

hkl	2θ [°]	q_z [Å^{-1}]	d_{001}
001	5.89	0.42	14.99
002	11.73	0.83	15.07
004	23.23	1.64	15.23
006	35.25	2.47	15.26

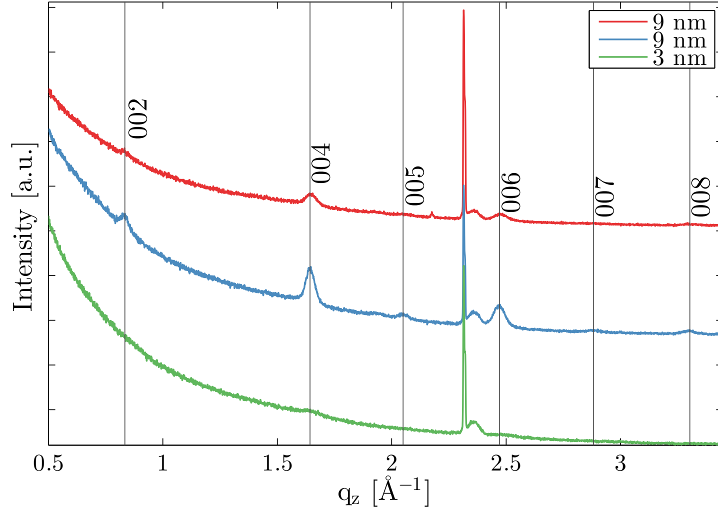

Figure 4.11: Specular X-ray diffraction for two samples with 9 nm and one sample with 3 nm thickness on SiO_2

calculated for every peak individually. The mean is (15.2 ± 0.1) Å which fits with the long molecular axis of Tyrian purple. The peak at $q_z = 2.3\,\text{Å}^{-1}$ is an artifact from the measurement. It is the $\frac{\lambda}{2}$-peak of d_{004} of silicon and occurs in all specular scans at this value.

Grazing incidence X-ray diffraction

One sample with 9 nm and one with 1.5 nm of Tyrian purple were measured with grazing incidence X-ray diffraction with incident angles $\alpha_\mathrm{i} = 0.09°$ and $\alpha_\mathrm{i} = 0.06°$, respectively. The reciprocal space maps are shown in Figure 4.12 and 4.13.
For the thicker sample (Figure 4.12), the measurement shows three rods with peaks smeared out along the rods. The unit cell was determined using the software PyGid. The unit cell parameters are $a = 3.85\,\text{Å}$, $b = 5.85\,\text{Å}$, $c = 15.22\,\text{Å}$, $\alpha = 98.9°$, $\beta = 94.0°$, $\gamma = 86.7°$, which is a triclinic cell. The volume is $V = 337.45\,\text{Å}^3$. In the bulk cell of Tyrian purple there are two molecules with a cell volume of $686.6\,\text{Å}^3$ [9]. This gives a volume of $343.3\,\text{Å}^3$ needed for one molecule, which compares quite well to the $337.45\,\text{Å}^3$ found for the surface induced phase. This means, that there is just one molecule per triclinic unit cell. The cell could be twice as large, containing

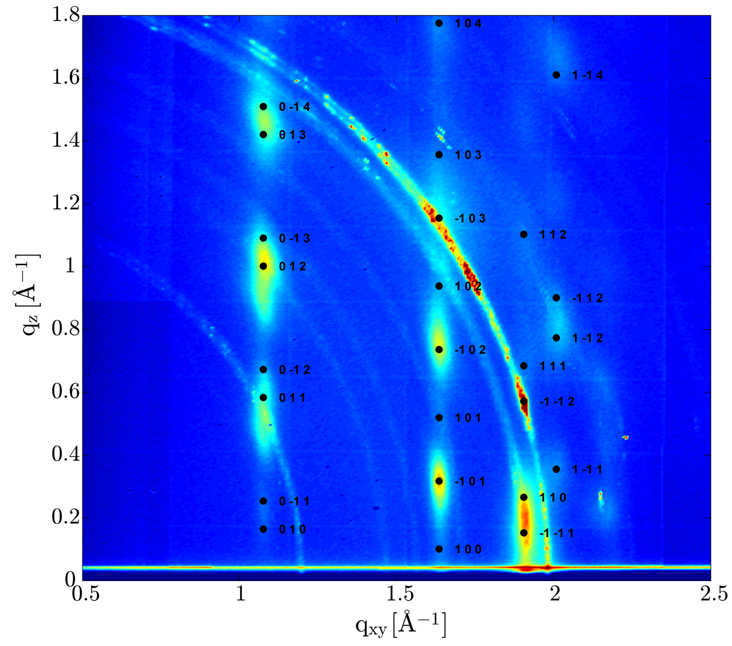

Figure 4.12: Reciprocal space map for 9 nm sample of Tyrian purple on SiO_2 with indexed cell. The unit cell parameters are $a = 3.85$ Å, $b = 5.85$ Å, $c = 15.22$ Å, $\alpha = 98.9°$, $\beta = 94.0°$, $\gamma = 86.7°$.

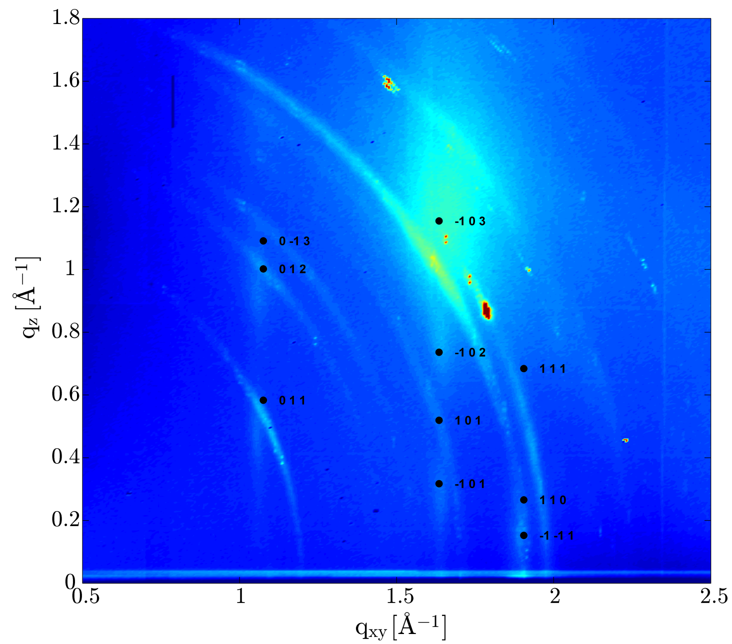

Figure 4.13: Reciprocal space map for 1.5 nm sample of Tyrian purple on SiO_2 with indexed cell. The unit cell paramters are $a = 3.85$ Å, $b = 5.85$ Å, $c = 15.22$ Å, $\alpha = 98.9°$, $\beta = 94.0°$, $\gamma = 86.7°$.

two molecules, but then there should be additional rods observed in the diffraction pattern.
Not all *hkl* indices are plotted, only those with a corresponding peak in the measurement. The contact plane with the substrate is 001, that is with the unit cell vectors **a** and **b** within the plane of the substrate, and **c** pointing upwards. The position of the first rod at $q_{xy} = 1.08\,\text{Å}^{-1}$ determines the unit cell parameter b^*, $b = 5.85\,\text{Å}$ being the real space equivalent to $1.08\,\text{Å}^{-1}$. Likewise, the second rod at $q_{xy} = 1.63\,\text{Å}^{-1}$ corresponds to the unit cell parameter a^*. The unit cell parameter c^* shifts the diffraction pattern up and down, while the angles split positive and negative *hkl* peaks.
The thinner sample shows only very weak peaks. The indexation is the same as for the sample in Figure 4.12. The first rod is slightly shifted to the left, which means that the unit cell parameter b is somewhat bigger. Also the sample shows a few Debye-Scherrer rings [53] which means that not all crystallites have a strong preferred orientation with respect to the substrate but are oriented randomly. The area with high intensity at around q_{xy} =1.6 nm and q_z =1.2 nm is a peak from the SiO_2 substrate. $q = \sqrt{q_{xy}^2 + q_z^2} = 2\,\text{Å}^{-1}$ corresponds to a real space distance of 3.1 Å which is the length of the Si-Si bond [54].

4.2.2 On plasma etched SiO_2

Samples of different thicknesses were prepared on plasma etched silicon oxide. The X-ray reflectivity measurements are shown in Figure 4.14.
The measured curves are comparable to those on the conventionally cleaned silicon oxide. The Bragg peak broadens and loses intensity as the film gets thinner but again no monolayer was achieved. This means once more that island growth is preferred over films of uniform thickness. Table 4.3 gives the position of the Bragg peaks and the calculated values for the crystallite size. These are again only rough estimates obtained by the Scherrer equation (equation 2.1). For the 0.6 nm sample no peak position can be given and for the 0.9 nm sample it was not possible to extract a full width at half maximum. The critical angle lies between $q_{\alpha_C} = 0.02813\,\text{Å}^{-1}$, $\alpha_C = 0.198°$ and $q_{\alpha_C} = 0.02884\,\text{Å}^{-1}$, $\alpha_C = 0.203°$.

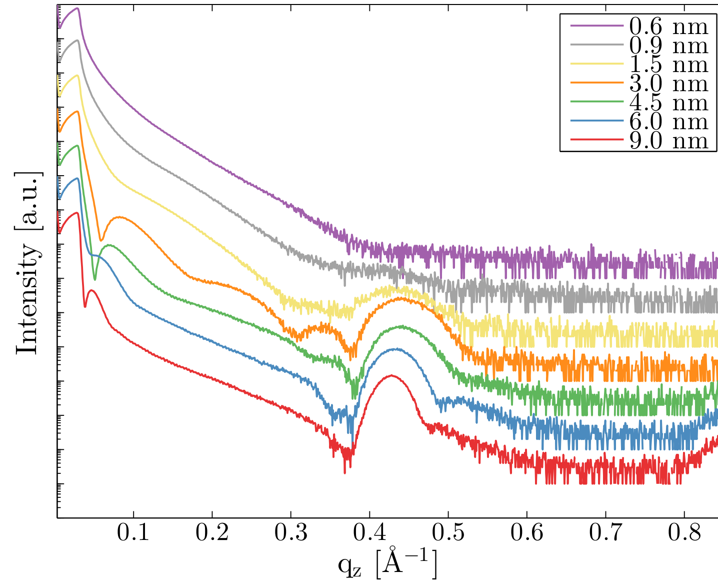

Figure 4.14: X-ray reflectivity for a series of samples with different film thicknesses on plasma etched silicon oxide

Table 4.3: Characteristic features of the X-ray reflectivity for different film thicknesses on plasma etched SiO_2: peak positions and estimates of crystallite size
2θ [°] ... position of Bragg peak
q_z [Å^{-1}] ... position of Bragg peak in reciprocal space
FWHM [°] ... full width at half maximum of Bragg peak
Λ [Å] ... estimate of crystallite size, calculated with equation 2.1

Sample	2θ [°]	q_z [Å^{-1}]	FWHM [°]	Λ [Å]
0.6 nm				
0.9 nm	5.86	0.417		
1.5 nm	5.98	0.426	1.04	80
3 nm	6.17	0.439	0.9	93
4.5 nm	6.15	0.438	0.79	106
6 nm	6.08	0.433	0.66	127
9 nm	6.01	0.428	0.52	159

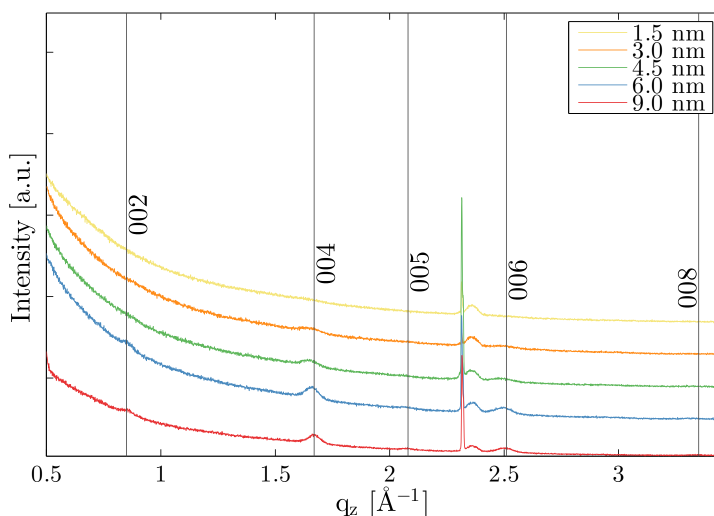

Figure 4.15: Specular X-ray diffraction for samples of different thicknesses on plasma etched SiO_2

Also the peak shift shows a similar pattern as on conventionally cleaned SiO_2. The peak shifts to larger values for decreasing film thickness and then to the lower values for samples of 1.5 nm and less. Since this pattern is observed twice, on different substrates, it is believed to be representing the real net plane distance in the films, which varies for different film thicknesses.

Specular X-ray diffraction

Specular X-ray diffraction was measured on these samples. The measured curves are plotted in Figure 4.15. They all have the same phase but with decreasing intensity as the samples get thinner. Table 4.4 gives the values of the measured Bragg peaks for the three thickest samples. Again, no 003 peak was observed. The intensity of the 007 peak was too low to give a specific peak position on all samples. The same applies for the empty cells in the table. For the thinner samples, the peaks have a too low intensity to allow the determination of exact peak positions. d_{001} gives the net plane distance calculated from the peak position.
As the samples get thinner, the peaks shift to smaller angles and thus larger net plane distances. When considering standing molecules on the

Table 4.4: Specular X-ray diffraction: Bragg peak positions of the surface induced crystal phase of Tyrian purple on plasma etched SiO_2 for samples of 9, 6 and 4.5 nm thickness
2θ [°] ... position of Bragg peak
q_z [$Å^{-1}$] ... position of Bragg peak in reciprocal space
d_{001} [Å] ... net plane distance

	9 nm			6 nm			4.5 nm		
hkl	2θ [°]	q_z [$Å^{-1}$]	d_{001} [Å]	2θ [°]	q_z [$Å^{-1}$]	d_{001} [Å]	2θ [°]	q_z [$Å^{-1}$]	d_{001} [Å]
001	6.09	0.43	14.50	6.01	0.43	14.68			
002	12.10	0.85	14.72	12.02	0.85	14.71			
004	23.63	1.67	15.04	23.51	1.66	15.12	23.21	1.64	15.31
005	29.48	2.08	15.13	29.24	2.06	15.25	29.17	2.05	15.29
006	35.77	2.51	15.04	35.70	2.50	15.07	35.29	2.47	15.24
008	48.49	3.35	15.00						

substrate, a smaller net plane distance would mean that the molecules are tilted slightly towards the substrate for the thicker samples, whereas they are more upright standing in the thinner films.

Grazing incidence X-ray diffraction

The samples of 1.5 nm and 9 nm thickness were investigated by grazing incidence X-ray diffraction. The reciprocal space maps are shown in Figure 4.16 and 4.17, respectively. The 1.5 nm sample was measured with an incident angle of $\alpha_\mathrm{i} = 0.06°$ and the 9 nm sample with $\alpha_\mathrm{i} = 0.075°$.
Again, the thinner sample shows only low intensity. Nevertheless, peaks are clearly distinguishable. The peaks are smeared out along the rod due to the small crystallite size in z-direction. There are also some Debye-Scherrer rings indicating that not all crystallites are oriented with respect to the substrate surface. The indexed cell is $a = 3.83$ Å, $b = 5.98$ Å, $c = 14.94$ Å, $\alpha = 94.4°$, $\beta = 92.7°$, $\gamma = 87.1°$, $V = 340.41\ Å^3$.
The 9 nm sample shows sharper peaks of higher intensity in both the z- and xy-direction, meaning that there are larger crystallites on the sample. The

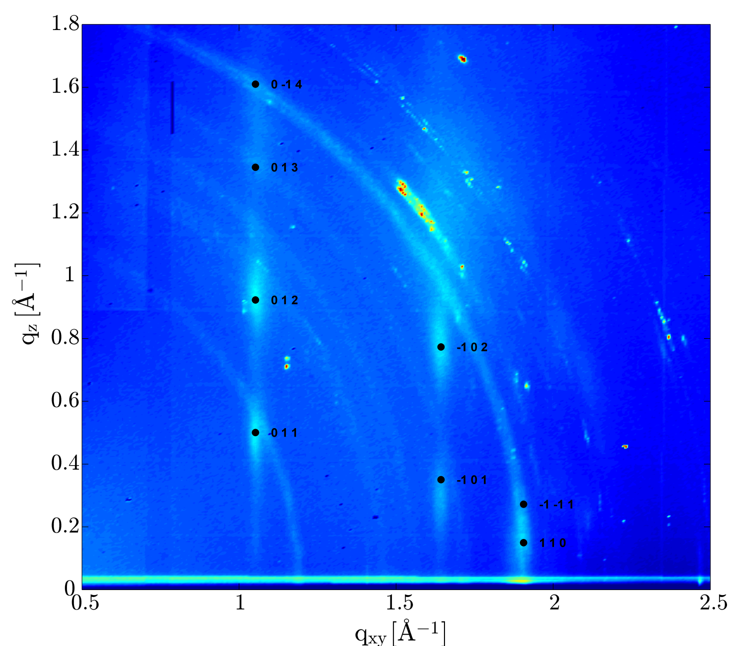

Figure 4.16: Reciprocal space map for 1.5 nm sample of Tyrian purple on plasma etched SiO_2 with indexed cell. The unit cell parameters are $a = 3.83$ Å, $b = 5.98$ Å, $c = 14.94$ Å, $\alpha = 94.4°$, $\beta = 92.7°$, $\gamma = 87.1°$.

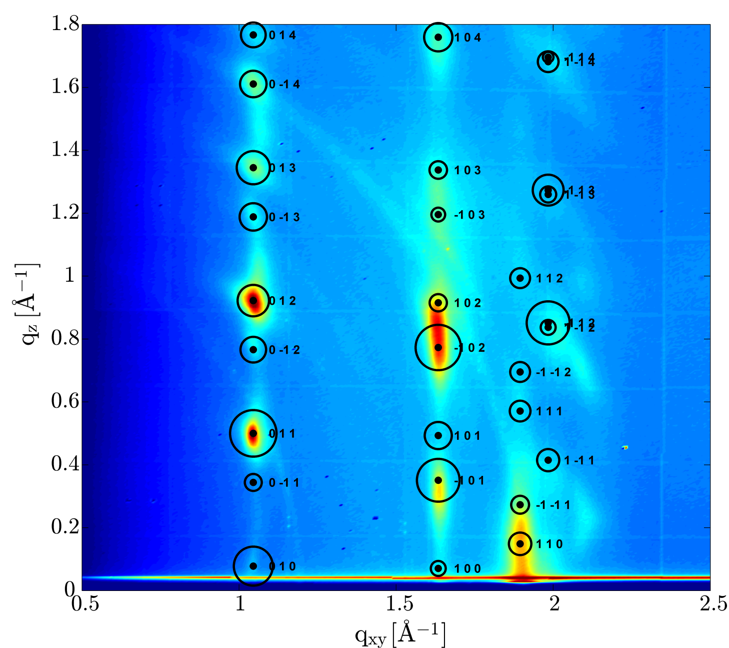

Figure 4.17: Reciprocal space map for 9 nm sample of Tyrian purple on plasma etched SiO_2 with indexed cell. The unit cell parameters are $a = 3.85$ Å, $b = 6.02$ Å, $c = 14.94$ Å, $\alpha = 94.4°$, $\beta = 92.7°$, $\gamma = 87.1°$. The black rings indicate the structure factors from the solved crystal structure.

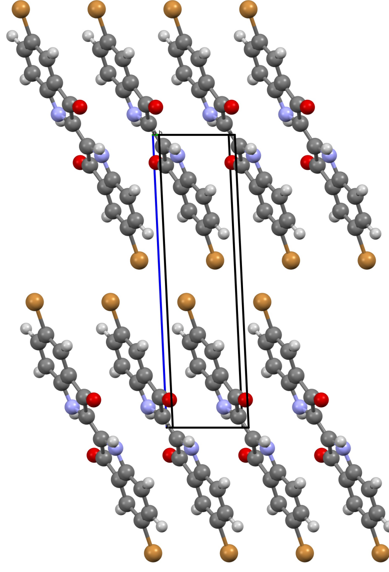

Figure 4.18: Calculated structure of Tyrian purple on plasma etched silicon oxide.

indexed cell in Figure 4.17 is $a = 3.85\,\text{Å}$, $b = 6.02\,\text{Å}$, $c = 14.94\,\text{Å}$, $\alpha = 94.4°$, $\beta = 92.7°$, $\gamma = 87.1°$, $V = 344.49\,\text{Å}^3$. With this unit cell the structure was simulated (see section 1.4.2). The rings in the map are a measure of the calculated structure factors. The larger the area of the rings the higher is the structure factor and thus the intensity which is proportional to the square of the structure factor. The agreement of the simulation with the measured intensity is quite good, especially in the first two rods and when it comes to the most intense peaks. Only at about $q_{xy} = 2\,\text{Å}^{-1}$ the agreement is not ideal. The structure and the packing is shown in Figure 4.18 with 001 plane on the horizontal, i.e. with the molecules standing as if on the substrate. The hydrogen bond length between the oxygen and nitrogen of two adjacent molecules is 2.817 Å compared to the sum of the van der Waals radii of 3.22 Å [55]. This shows, as expected, that the hydrogen bond is stronger than just a van der Waals bond. The distance between two bromine atoms of two molecules stacked on top of each other is 3.989 Å. This is slightly larger than the sum of the van der Waals radii, which is 3.74 Å. The distance between two parallel molecules is 3.272 Å. This was expected from the peaks at $q_{xy} = 1.9\,\text{Å}^{-1}$ in the reciprocal space maps.

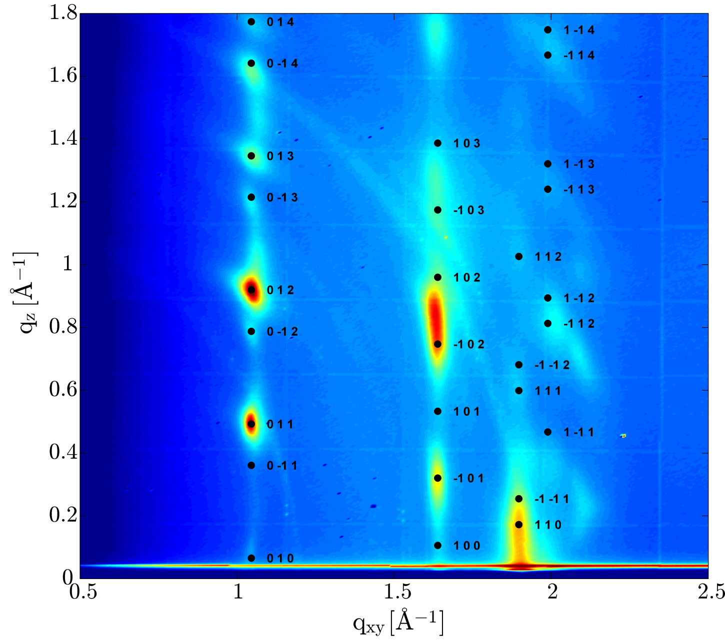

Figure 4.19: Reciprocal space map for 9 nm sample of Tyrian purple on plasma etched SiO_2. The indexed cell was calculated analytically, the unit cell parameters are $a = 3.84$ Å, $b = 6.02$ Å, $c = 14.78$ Å, $\alpha = 93.8°$, $\beta = 93.9°$, $\gamma = 87.0°$.

This reciprocal space map was also indexed analytically using equations 2.4. The 011, -101, 110, 012 and 0-13 peaks and their positions in q-space were used for the calculation. This gave a unit cell with the following parameters: $a = 3.84$ Å, $b = 6.02$ Å, $c = 14.78$ Å, $\alpha = 93.8°$, $\beta = 93.9°$, $\gamma = 87.0°$, $V = 339.45$ Å^3. The result is shown in Figure 4.19.
The parameters a, b and γ compare very well. The angles α and β differ just slightly. The lattice constant c shows the biggest difference. c is also the parameter which varies most between the samples on different substrates. The indexation for the first rod looks nearly identical, whereas the indexation for the second rod varies between the two unit cells, especially in the area around -102 and 102 where it is difficult to give the exact peak position.

4.2.3 Comparison

When comparing the measurements for samples on the two different SiO_2 substrates quantitatively, it becomes visible that the Bragg peaks are shifted

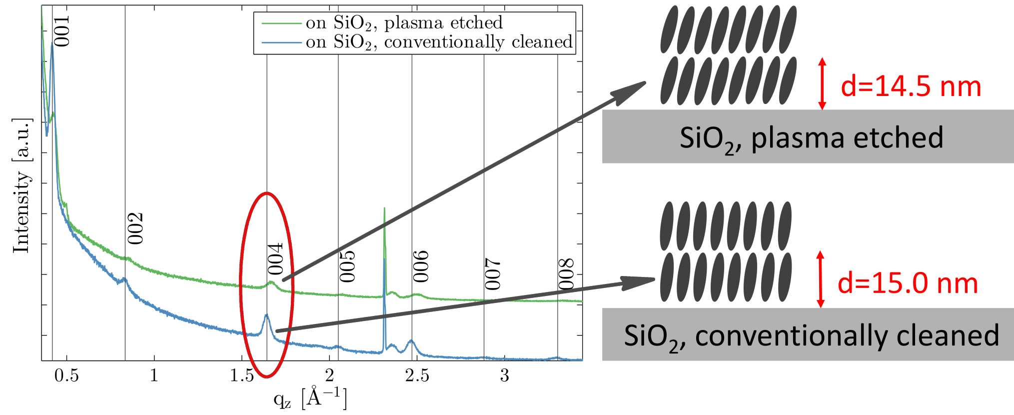

Figure 4.20: Specular X-ray diffraction for samples of 9 nm thickness on conventionally cleaned SiO_2 and plasma etched SiO_2 with a schematic drawing of the molecules on the substrate

with respect to each other. Two specular scans are shown in Figure 4.20 for the 9 nm samples.

The gray vertical lines mark the position of the peaks on the conventionally cleaned silicon oxide. The peaks for Tyrian purple on the plasma etched substrate are clearly shifted to higher q values. This means that the interplanar distance between two net planes of Tyrian purple is smaller on a plasma etched silicon oxide substrate than on the conventionally cleaned silicon oxide. Assuming standing molecules, a smaller interplanar distance would mean that the molecules have a larger tilt towards the substrate. A schematic drawing illustrating this is shown on the right in Figure 4.20. The reason is most likely the surface energy. The plasma etched SiO_2 has a higher surface energy, combining a higher dispersive part and a higher polar part (see Table 3.1). Thus, it is more hydrophilic than the conventionally cleaned SiO_2. The strong hydrogen bonding within and between Tyrian purple molecules makes them lean more towards the hydrophilic substrate and stand more upright on the rather hydrophobic substrate.

When comparing the grazing incidence X-ray diffraction maps of the two 9 nm samples, differences can be seen, though the overall pattern is the same. The unit cells differ slightly. The parameters a and b are different for the two maps as a result of the difference in the positions of the first two rods. The parameter c is higher for the unit cell on the conventionally cleaned SiO_2 and lower for the plasma etched SiO_2. This is in agreement with what was found from the specular scans and is depicted in Figure 4.20. On the plasma etched SiO_2, the peaks are sharper in z-direction which means that the crystallites are larger in this direction than on the conventionally cleaned silicon oxide.
What both maps have in common is the peak at $q_{xy} = 1.9\,\text{Å}^{-1}$ and $q_z = 0$–$0.3\,\text{Å}^{-1}$. This corresponds to a real space distance of 3.3 Å, which is the spacing between two aromatic rings of two adjacent molecules [56]. This is another indicator that Tyrian purple packs in parallel stacks of standing molecules. This peak will also be prominent in all reciprocal space maps in the following chapter.

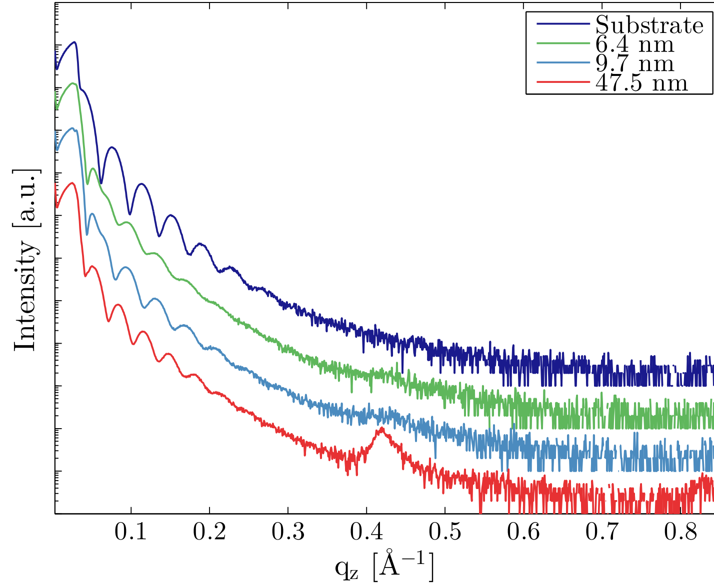

Figure 4.21: X-ray reflectivity measurements for different thicknesses of Tyrian purple on an EGDMA substrate

4.3 Surface induced phase on other substrates

4.3.1 EGDMA (Ethylene glycol dimethacrylate)

Samples of 47.5, 9.7 and 6.4 nm thickness were prepared on the EGDMA substrate. Again, the given thicknesses are to be understood as nominal thicknesses of the Tyrian purple films. The samples were measured with X-ray reflectivity. Figure 4.21 shows the results, also in comparison to the pure substrate (dark blue).

Specular X-ray diffraction was also measured (Figure 4.22). The two thinner samples hardly show any Bragg peaks, whereas the thickest sample (47.5 nm) has pronounced diffraction peaks. The peak positions match the surface induced phase as measured on SiO_2. These are indicated by vertical lines in the figure. However, there is a strong unknown peak at $q_z = 1.94\,\text{Å}^{-1}$, $2\theta = 27.48°$. It does not fit to the Tyrian purple bulk cell with the closest peak, the 004 peak, at $q_z = 2.06\,\text{Å}^{-1}$, $2\theta = 29.2°$ [9]. Also, it does not correspond to the surface induced phase on copper iodide, which

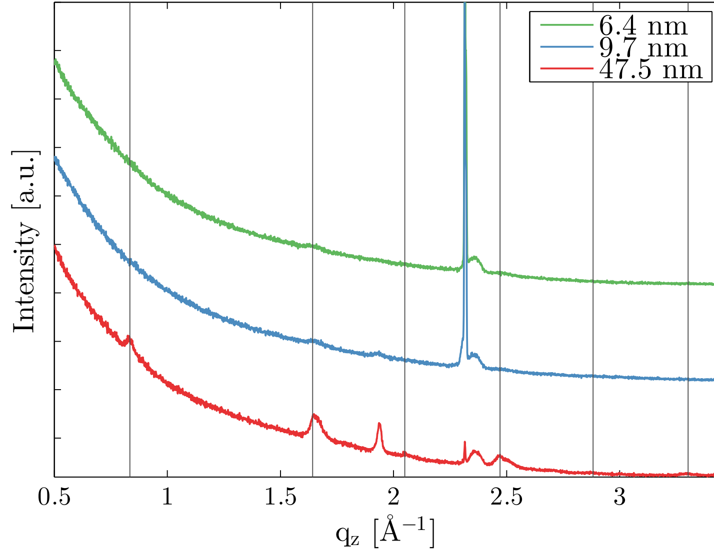

Figure 4.22: Specular X-ray diffraction measurements for different thicknesses of Tyrian purple on an EGDMA substrate. The vertical lines indicate the position of the Bragg peaks of the surface induced phase.

was observed in an orientation with lying molecules on the substrate [10]. The thickest sample was measured by grazing incidence X-ray diffraction (Figure 4.23) with an incident angle of $\alpha_i = 0.07°$. The main features of this map are the peaks which are smeared out along the Debye-Scherrer rings. This means again that there are some crystallites, which are not perfectly aligned to the substrate with the contact plane (001), but deviate somewhat from this orientation. There are also some rings which are nearly continuous, which indicates that there are also crystallites with a random orientation.

The map was indexed using PyGid with the following unit cell: $a = 3.85\,\text{Å}$, $b = 6.20\,\text{Å}$, $c = 14.92\,\text{Å}$, $\alpha = 94.0°$, $\beta = 91.5°$, $\gamma = 88.9°$, $V = 355.11\,\text{Å}^3$. The parameters a and c correspond to those of Tyrian purple on plasma etched SiO_2. However, the parameter b is larger, which also accounts for the larger unit cell volume of $355.11\,\text{Å}^3$, which is about 3 % larger than on plasma etched SiO_2.

This unit cell was used to calculate the powder pattern. The -110 peak is at a position $q = 1.939\,\text{Å}^{-1}$ which is also the position of the so far unknown peak in the specular scan. Seeing additional peaks apart from the $00l$ series,

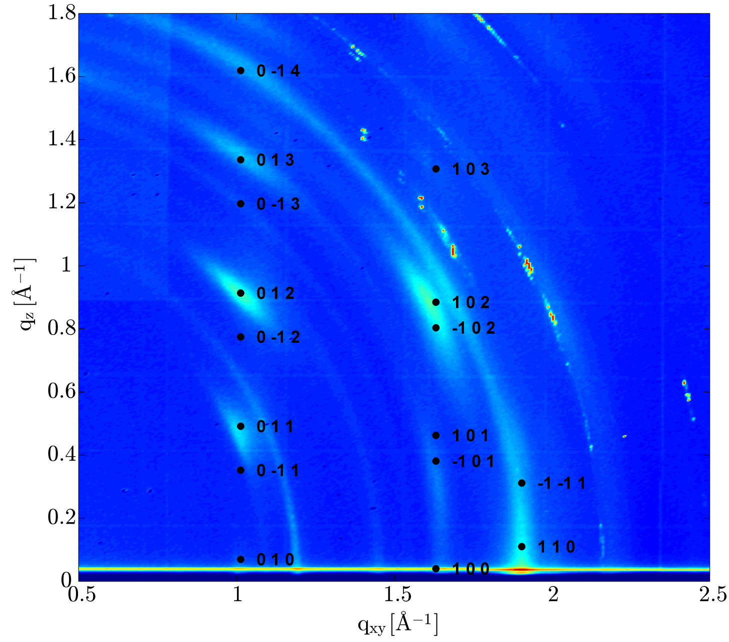

Figure 4.23: Grazing incidence X-ray diffraction for the 47.5 nm sample on the EGDMA substrate. The indexed unit cell is $a = 3.85$ Å, $b = 6.20$ Å, $c = 14.92$ Å, $\alpha = 94.0°$, $\beta = 91.5°$, $\gamma = 88.9°$

suggests that there is another orientation present on the sample, in this case (-110). It might also be the 11-1 peak, which has a q value of 1.929 Å^{-1}. However, whichever orientation it is, the peak at $q = 1.94$ Å^{-1} corresponds to a real space distance of 3.24 Å. Considering the dimensions of the molecule this must be a flat-on orientation towards the substrates, meaning that the molecules lie on the substrate with the aromatic rings parallel to the substrate surface.

4.3.2 HMDSO (Hexamethyldisiloxane)

Two samples were prepared on the HMDSO substrate with a thickness of 9 nm and 18.4 nm, respectively. Figure 4.24 shows their X-ray reflectivity curves together with the substrate reflectivity. Again two critical angles are distinguishable. As the thickness of the film increases, the Kiessig fringes of the pure substrate decrease earlier. For the thinner sample the Bragg peak at $q = 0.42$ Å^{-1} is hardly observable, whereas, for the thicker sample,

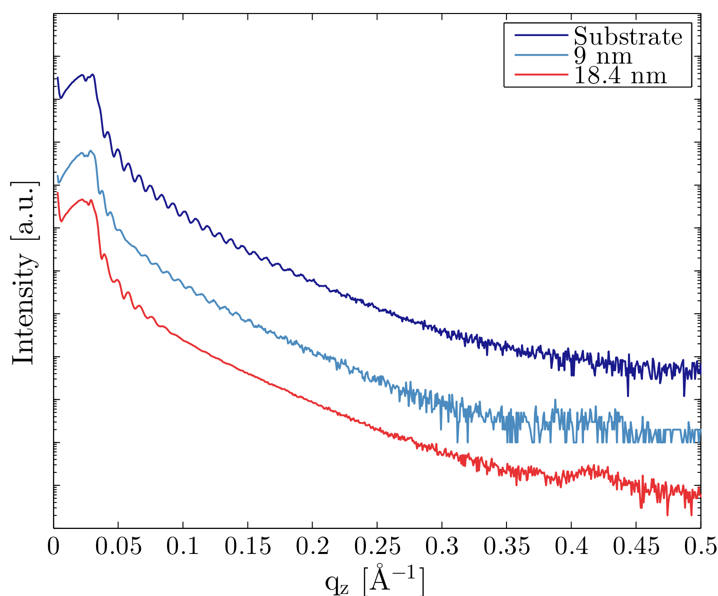

Figure 4.24: X-ray reflectivity measurements for different thicknesses of Tyrian purple on an HMDSO substrate

it is clearly recognizable. The same was the case with samples on the EGDMA substrate, which is why thicker samples were prepared on the polymer substrates than on the SiO_2 substrates.

Figure 4.25 shows the specular X-ray diffraction measurements for these two samples. Again there are no diffraction peaks visible for the thin sample, but the tick sample shows peaks of the surface induced crystal phase.

The grazing incidence diffraction measurement for the 18.4 nm sample is shown in Figure 4.26. The incidence angle was $\alpha_i = 0.08°$. Again the map shows some rings and peaks, indicating that there are both oriented and disoriented Tyrian purple crystallites formed on this substrate. The unit cell parameters are $a = 3.84$ Å, $b = 5.78$ Å, $c = 15.16$ Å, $\alpha = 95.3°$, $\beta = 93.6°$, $\gamma = 86.5°$ which give a volume of $V = 333.89$ Å^3. This is by a couple of Å^3 smaller than for previous samples. The reason might be that this substrate is much more hydrophobic than the substrates so far (see Table 3.1) and this causes the Tyrian purple molecules to pack more densely.

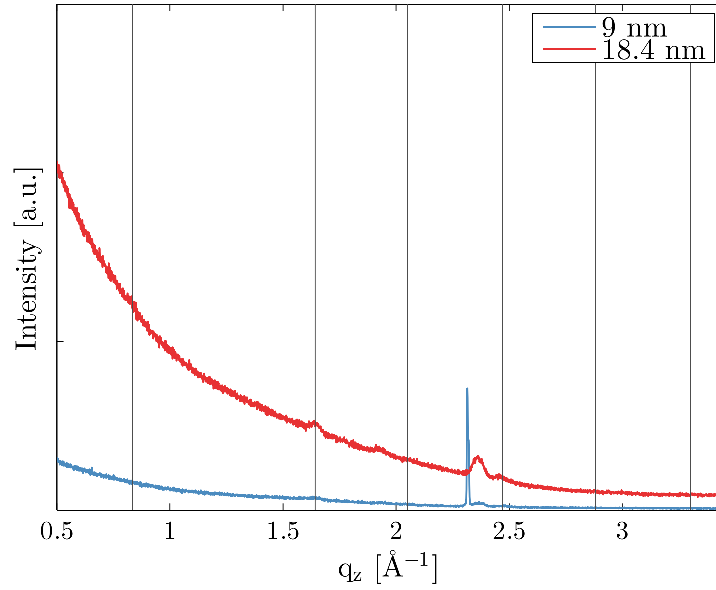

Figure 4.25: Specular X-ray diffraction measurements for different thicknesses of Tyrian purple on an HMDSO substrate. The vertical lines indicate the position of the Bragg peaks of the surface induced phase.

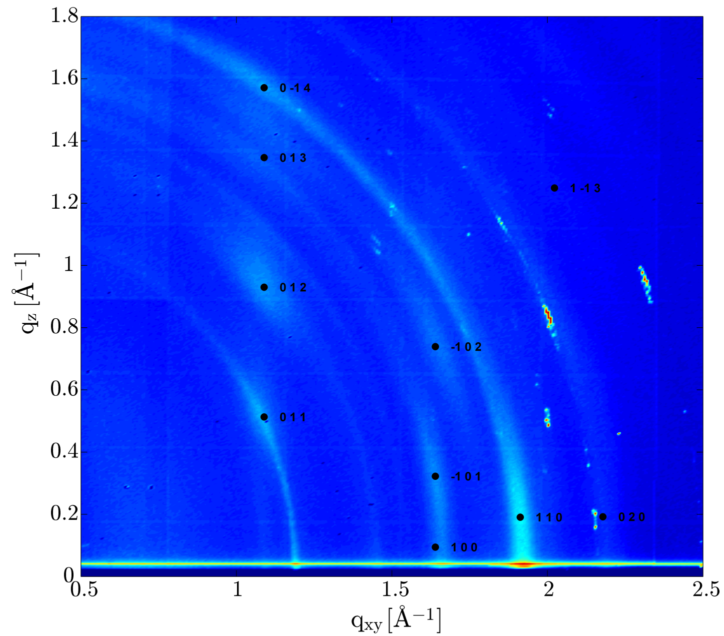

Figure 4.26: Grazing incidence X-ray diffraction for the 18.4 nm sample on the HMDSO substrate. The indexed unit cell is $a = 3.84$ Å, $b = 5.78$ Å, $c = 15.16$ Å, $\alpha = 95.3°$, $\beta = 93.6°$, $\gamma = 86.5°$

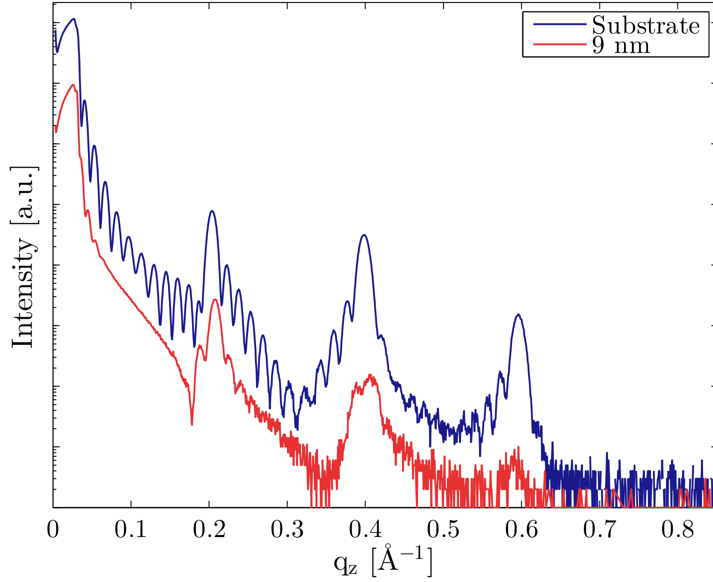

Figure 4.27: X-ray reflectivity measurements for different thicknesses of Tyrian purple on a PFDA substrate

4.3.3 PFDA (1H, 1H, 2H, 2H,-perfluorodecyl acrylate)

Figure 4.27 shows the X-ray reflectivity measurement of a Tyrian purple sample with 9 nm nominal thickness on PFDA in comparison with the pure PFDA substrate. The Tyrian purple film increases the surface roughness of the sample, which strongly decreases the Kiessig fringes as a result. The diffraction peaks of PFDA are still very dominant but also decreased in intensity.

Specular X-ray diffraction was also measured, but did not show clear diffraction peaks from Tyrian purple but only from PFDA. There were not enough Tyrian purple crystallites with a preferred orientation to the substrate to get a detectable intensity in a $\theta/2\theta$-scan.

Grazing incidence X-ray diffraction was also measured on this sample with $\alpha_i = 0.06°$. The reciprocal space map is shown in Figure 4.28. Indeed, it shows a lot of rings originating from randomly oriented crystallites. Additionally, there are also a couple of peaks along the rods. The indexation gave the following unit cell: $a = 3.84$ Å, $b = 5.78$ Å, $c = 15.12$ Å, $\alpha = 95.3°$,

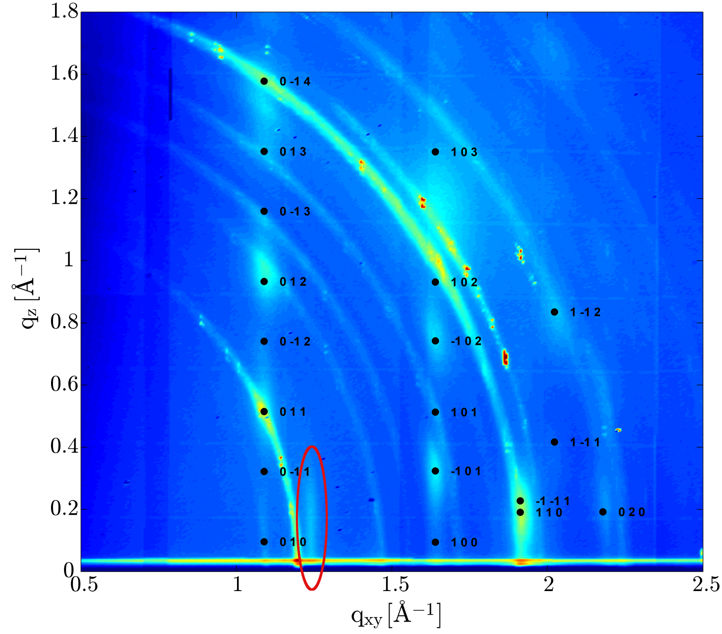

Figure 4.28: Grazing incidence X-ray diffraction for a 9 nm sample on the PFDA substrate. The indexed unit cell is a = 3.84 Å, b = 5.78 Å, c = 15.12 Å, α = 95.3°, β = 93.7°, γ = 86.5°. The rod circled in red is a feature of the structure of the PFDA substrate.

β = 93.7°, γ = 86.5°. This, again, has a comparatively low volume of V = 332.97 Å^3. The unit cell is also very similar to the one for the sample on HMDSO. This is not surprising as the PFDA polymer substrate is even more hydrophobic than the HMDSO polymer. The circled rod at q_{xy} = 1.24 Å^{-1} and q_z = 0–0.3 Å^{-1} is a feature of the structure of PFDA.

4.4 Surface energy dependence of the surface induced phase

All unit cells, which were found by indexing the reciprocal space maps measured by grazing incidence X-ray diffraction, have varying unit cell parameters and volumes. Table 4.5 gives an overview of these cells. The substrates are arranged from left to right with decreasing surface energy, thus increasing hydrophobicity.

Table 4.5: Overview of the unit cell parameters of Tyrian purple on different substrates. The surface energy of the substrate decreases from left to right. d [nm] ... nominal sample thickness

	SiO_2 plasma etched		SiO_2 conventionally cleaned		EGDMA	HMDSO	PFDA
d [nm]	9.0	1.5	9.0	1.5	47.5	18.4	9.0
a [Å]	3.85	3.83	3.85	3.85	3.85	3.84	3.84
b [Å]	6.02	5.98	5.85	5.85	6.20	5.78	5.78
c [Å]	14.94	14.94	15.22	15.22	14.92	15.16	15.12
α [°]	94.4	94.4	98.9	98.9	94.0	95.3	95.3
β [°]	92.7	92.7	94.0	94.0	91.5	93.6	93.7
γ [°]	87.1	87.1	86.7	86.7	88.9	86.5	86.5
V [Å^3]	344.49	340.41	337.45	337.45	355.11	333.89	332.97

Not only the unit cell parameters vary, but also the volume does. It decreases as the surface energy decreases, which means that Tyrian purple packs more densely on hydrophobic surfaces.

The lattice constant a stays nearly constant, but b and c follow certain trends as the surface energy decreases. The constant b decreases as well, whereas c increases. However, the unit cell for Tyrian purple on EGDMA stands out, not following this relation and also having a volume much higher than the others. Because the peaks are so smeared out in the reciprocal space map (Figure 4.23), it was difficult to find an indexation and the one given might not represent the real unit cell.

Since the lattice constant c increases with decreasing surface energy, and it is the one pointing out-of-plane, this suggests that the molecules stand more upright on a more hydrophobic substrate. This was also observed by comparing the specular X-ray diffraction scans measured for Tyrian purple on the two different SiO_2 substrates (see section 4.2.3).

Figure 4.29 shows the surface energy dependence of the net plane distance parallel to the substrate normal. The net plane distance calculated from the first Bragg peak in the X-ray reflectivity curves was used to represent

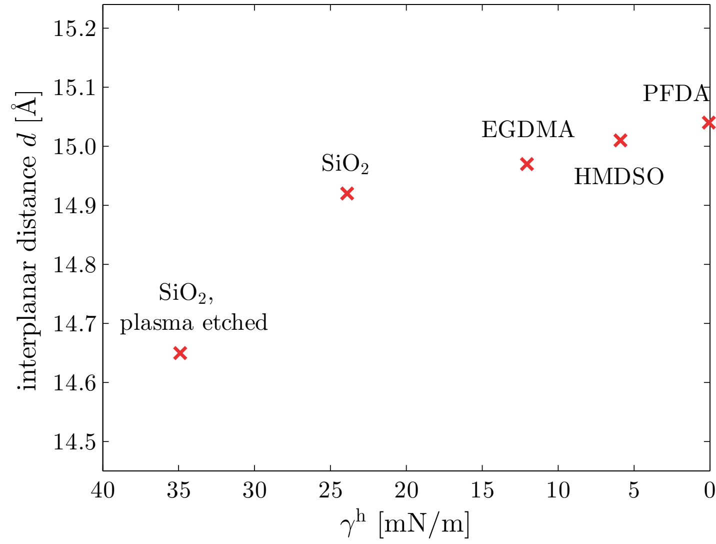

Figure 4.29: Surface energy dependence of the net plane distance of Tyrian purple on substrates of different surface energies

this correlation. Only the value for Tyrian purple on the PFDA substrate was calculated from the unit cell, as the peaks of the PFDA overlay those of Tyrian purple and so no exact position can be extracted from XRR. This also shows that molecules are tilted more towards the substrate when the surface is hydrophilic and tilted less on a hydrophobic surface.
However, despite the varying unit cells and diffraction patterns, one feature remains constant on all reciprocal space maps. This is the peak at $q_{xy} = 1.9\,\text{Å}^{-1}$ and $q_z = 0\text{–}0.3\,\text{Å}^{-1}$. As already discussed in section 4.2.3 this corresponds to a real space distance of 3.3 Å. This is the known distance between two aromatic rings of two parallel molecules [56]. Together with the overall unit cell dimensions and what was found from X-ray reflectivity, this suggests that Tyrian purple packs in parallel stacks of standing molecules.

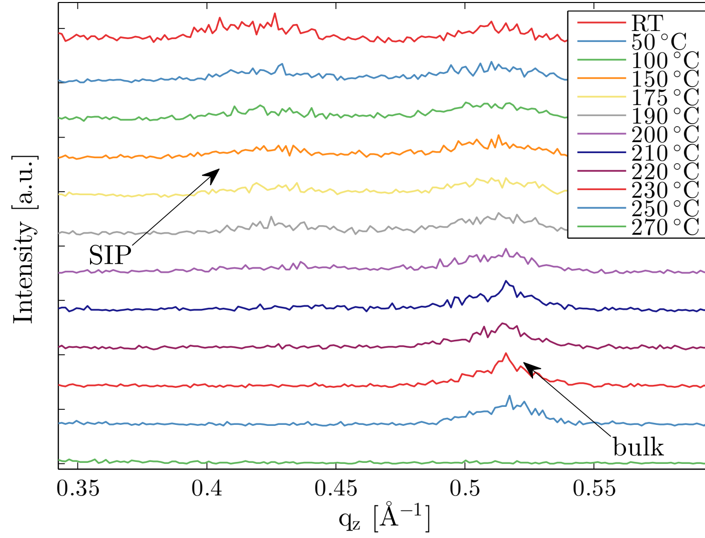

Figure 4.30: Heating experiment for a sample of Tyrian purple prepared by hot wall epitaxy at 100 °C substrate temperature on SiO_2

4.5 Thermal stability

The thermal stability of Tyrian purple was investigated using specular X-ray diffraction in combination with a heating stage. The samples were measured first at room temperature. Then the temperature was increased in discrete steps. After the desired temperature was reached a diffraction measurement was performed, which took 12 to 15 min depending on the intensity of a sample. Then the sample was heated further and measured again, and so forth.

Figure 4.30 shows an example of such an experiment. This sample was prepared by hot wall epitaxy at 100 °C substrate temperature on silicon oxide. The specular X-ray diffraction was shown in Figure 4.2.

At room temperature two peaks are measured. The one at $q_z = 0.42\,\text{Å}^{-1}$ is from the surface induced phase and the one at $q_z = 0.51\,\text{Å}^{-1}$ is from the bulk phase. As the temperature increases, the peak of the surface induced phase decreases in intensity while the bulk peak remains at the same intensity, but the peak gets a little sharper. This suggests that the surface induced phase undergoes a phase transition to the bulk phase, which is completed at about 200 °C. A sharper peak for the bulk phase means that the crystallite size

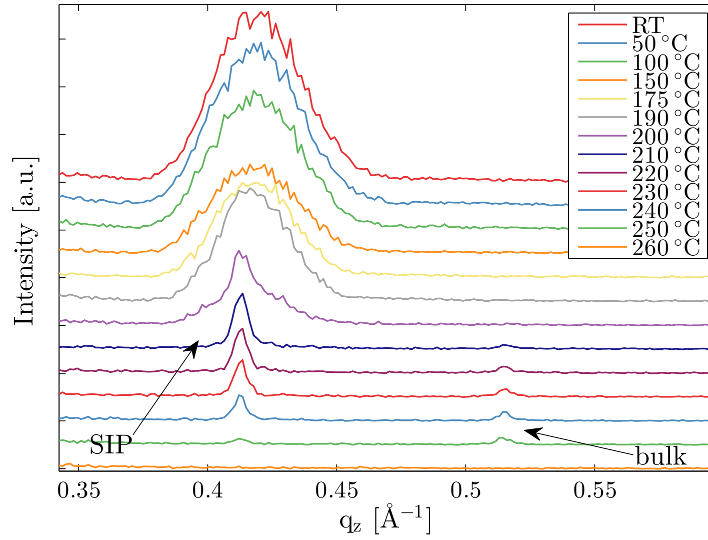

Figure 4.31: Heating experiment for a 9 nm sample of Tyrian purple on conventionally cleaned SiO_2

perpendicular to the surface increases with increasing temperatures. Above 250 °C no signal was measured anymore. This could have been a result of Tyrian purple melting at that temperature, however, also after cooling down, no intensity could be measured. Upon removing the sample from the diffractometer, it was observed that the film was gone from the substrate, which means that it must have completely sublimated at a temperature between 250 °C and 270 °C. Sublimation was also observed when attempting to measure differential scanning calorimetry on the Tyrian purple powder. The sublimation made it impossible to perform the measurement.

Another experiment is shown in Figure 4.31. It shows a sample on conventionally cleaned silicon oxide with a nominal thickness of 9 nm of Tyrian purple. The X-ray reflectivity of this sample is shown in Figure 4.9 and the specular diffraction in Figure 4.11 (in blue), respectively.

At room temperature only the surface induced phase is found on this sample. At 200 °C to 210 °C a phase transition from the surface induced phase to the bulk phase is observed. In the same temperature range the peak from the surface induced phase jumps to a much smaller width and lower intensity. A smaller width indicates a larger crystallite size, however, also the intensity decreases such that the area under the peak is considerably smaller, which means that there is less material on the sample. This sug-

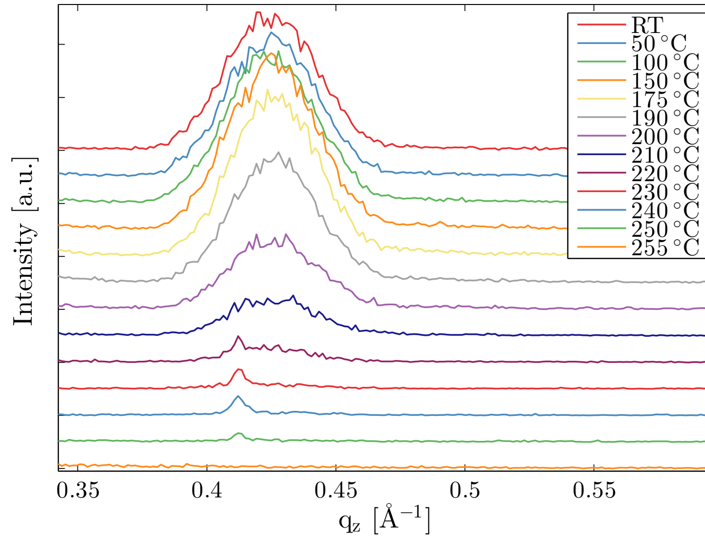

Figure 4.32: Heating experiment for a 9 nm sample of Tyrian purple on plasma etched SiO_2

gests that the sublimation starts at a lower temperature and is accelerated as the temperature increases further. Again, above 250 °C no Tyrian purple was measured on the sample.
The same experiment was performed on a sample of 9 nm nominal thickness on plasma etched silicon oxide. The results are shown in Figure 4.32.
In this measurement no phase transition was observed. Nevertheless, the peak of the surface induced phase shows the same behavior as in the previous measurement. There were further experiments performed on samples on conventionally cleaned SiO_2, where no phase transition was observed. So this is not necessarily a result of plasma etching the substrate and thus making it more hydrophilic. The reason why a phase transition occurs on some samples and not on others is not yet fully understood. However, for all samples with both the surface induced phase and the bulk phase present in the as-prepared state, a phase transition was observed.
This was, for example, the case for Tyrian purple on polyethylene prepared by hot wall epitaxy at 100 °C. Figure 4.1 showed the specular scan for this sample in blue. As can be seen, there are both phases, but the surface induced phase is dominant. The heating experiment is shown in Figure 4.33. This time the sample was not heated until sublimation, but the heating was stopped at 210 °C and the sample was cooled down at the same rate as

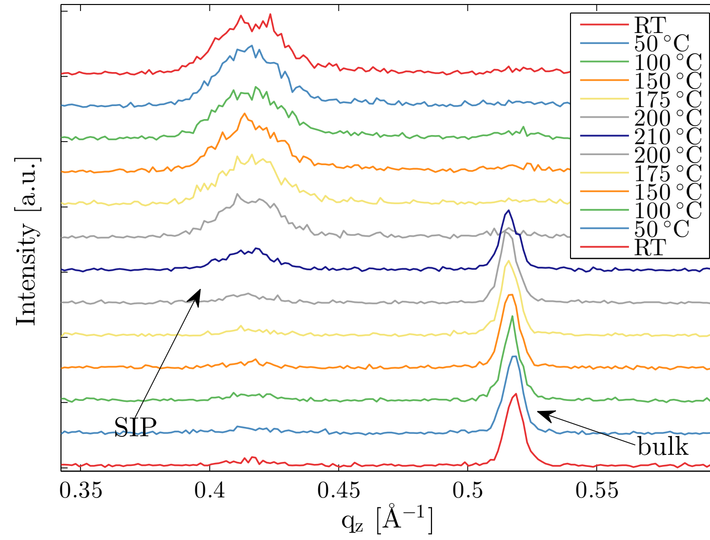

Figure 4.33: Heating experiment for a sample of Tyrian purple on polyethylene, prepared by hot wall epitaxy at 100 °C substrate temperature

heated up. A measurement was performed at each temperature step. Again, the peak of the surface induced phase loses intensity as the sample is heated up. At a temperature of 210 °C the phase transition to the bulk phase occurs. While cooling down the sample this peaks remains the same. The surface induced phase still decreases slightly in intensity, but nevertheless, after reaching room temperature there is some surface induced phase left. This shows clearly that the bulk phase is the thermodynamically stable phase, while the surface induced phase is metastable. It either changes to the bulk phase at elevated temperatures or it sublimates directly.

5 Conclusion

Tyrian purple has become interesting for its semiconducting properties. In thin films, which are needed for electronic devices, it forms another polymorphic phase, which had not previously been investigated. Samples prepared by hot-wall-epitaxy at different substrate temperatures were analyzed. It was found that the thin film phase (surface induced phase) is dominant when prepared at lower temperatures and the bulk phase prevails at higher temperatures. Further sample preparation was performed by thermal vapor deposition with the substrates kept at room temperature.
On samples prepared at room temperature only the surface induced phase was found. X-ray reflectivity measurements and their corresponding fits show that the sample surface is very rough, because of islands forming on the substrates. Within these islands molecules are standing, packed parallel to each other. On two polymer substrates specular X-ray reflectivity exhibits an additional peak, originating from a flat-on orientation of the molecules. Grazing incidence diffraction was measured on samples on different substrates. All reciprocal space maps were indexed with unit cells. They all have very similar parameters, but are not exactly the same. They are all triclinic with one molecule per unit cell, which is significantly different from the monoclinic bulk phase with two molecules in the unit cell. An overview of the unit cell parameters is given in Table 4.5. The parameter a is nearly constant while b and c vary to some extend. The different substrates all have different surface energy. With the exception of one sample they show a clear trend of decreasing b and increasing c as the substrate gets more hydrophobic. Also the volume decreases as the surface energy decreases. The molecules pack more densely and stack more upright on hydrophobic substrates. This was also found from specular scans on silicon oxide substrates of different surface energy. The reason for this is most likely the strong inter- and intra-molecular hydrogen bonding in Tyrian purple. A peak at

$q_{xy} = 1.9\,\text{Å}^{-1}$ and $q_z = 0\text{–}0.3\,\text{Å}^{-1}$ is very prominent on all reciprocal space maps. It corresponds to the distance between two aromatic rings of parallel molecules, which is another indicator for the parallel stacking of standing molecules. A structure solution was calculated for Tyrian purple on plasma etched silicon oxide, which confirms this molecular packing. A schematic drawing of the packing in the bulk and on two substrates of different surface energy is shown in Figure 5.1.
The thermal stability of the surface induced phase was investigated by measuring specular X-ray diffraction at different temperatures. For samples with both the bulk and surface induced phase present in the as-prepared state a phase transition from the surface induced phase to the bulk was observed at 210 °C. It was also found that Tyrian purple sublimates at temperatures higher than 250 °C. Some samples with just the surface induced phase sublimated without a phase transition while on other samples a phase transition to the bulk phase occurred. On samples which were cooled down right after the phase transition, the bulk phase remained. This shows that the bulk phase is indeed the thermodynamically stable while the surface induced phase is metastable.

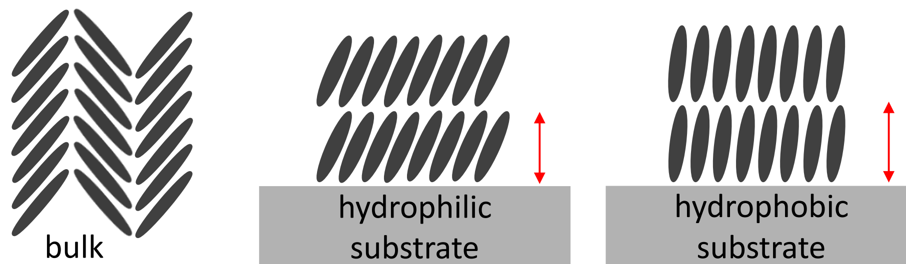

Figure 5.1: Schematic drawing of the packing of Tyrian purple in the bulk (left), on a hydrophilic substrate (middle) and on a hydrophobic substrate (right)

List of Figures

1.1 Chemical structure of Tyrian purple (6,6'-dibromoindigo) . . 2
1.2 Crystal bulk structure of Tyrian purple 3
1.3 Schematic drawing of the crystal bulk phase versus the surface induced phase 6

2.1 Setup used for the sample preparation 14
2.2 Schematic drawing of specular X-ray diffraction 15
2.3 Measurement setup of the diffractometer 16
2.4 Schematic drawing of X-ray reflectivity 17
2.5 Influence of sample parameters on X-ray reflectivity curves . 18
2.6 Schematic drawing of grazing incidence X-ray diffraction . . 20
2.7 Grazing incidence X-ray diffraction - cross section of the reciprocal space 21

3.1 Chemical structures of EGDMA, HMDSO and PFDA 24
3.2 Schema of a contact angle measurement 25
3.3 X-ray reflectivity measurement of the EGDMA substrate . . 27
3.4 Atomic force microscopy image of the EGDMA substrate . . 28
3.5 X-ray reflectivity measurement of the HMDSO substrate . . 29
3.6 Atomic force microscopy image of the HMDSO substrate . . 29
3.7 X-ray reflectivity measurement and fit of the PFDA substrate 30
3.8 Calculated electron density of the PFDA substrate 31
3.9 Atomic force microscopy image of the PFDA substrate surface 31

4.1 XRD - Tyrian purple on polyethylene 35
4.2 XRD - Tyrian purple on silicon oxide 36
4.3 XRD - Tyrian purple on silicon oxide 36
4.4 Reciprocal space map: Tyrian purple on SiO_2, 100 °C sample 38

4.5 Reciprocal space map: Tyrian purple on SiO_2, 150 °C sample 38
4.6 X-ray reflectivity of a 9 nm sample 39
4.7 XRR for a sample of 9 nm - comparison with fit 40
4.8 Normalized electron density for a 9 nm sample 41
4.9 XRR for different film thickness on SiO_2 42
4.10 Schematic of standing molecules on a substrate 43
4.11 XRD for Tyrian purple on SiO_2 45
4.12 GIXD for 9 nm Tyrian purple on SiO_2 46
4.13 GIXD for 1.5 nm Tyrian Purple on SiO_2 46
4.14 XRR for different film thickness on plasma etched SiO_2 . . . 48
4.15 XRD for Tyrian purple on plasma etched SiO_2 49
4.16 GIXD for 1.5 nm Tyrian purple on plasma etched SiO_2 . . . 51
4.17 GIXD for 9 nm Tyrian Purple on plasma etched SiO_2 with solved crystal structure 51
4.18 Calculated structure of Tyrian purple on plasma etched SiO_2 52
4.19 GIXD for 9 nm Tyrian Purple on plasma etched SiO_2, analytical indexation 53
4.20 Comparison of XRD measurements on two SiO_2 substrates . 54
4.21 XRR for Tyrian purple on EGDMA 56
4.22 XRD for Tyrian purple on EGDMA 57
4.23 GIXD for Tyrian purple on EGDMA 58
4.24 XRR for Tyrian purple on HMDSO 59
4.25 XRD for Tyrian purple on HMDSO 60
4.26 GIXD for Tyrian purple on HMDSO 60
4.27 XRR for Tyrian purple on PFDA 61
4.28 GIXD for Tyrian purple on PFDA 62
4.29 Surface energy dependence of the net plane distance 64
4.30 Heating experiment for a sample prepared by hot wall epitaxy on SiO_2 65
4.31 Heating experiment for a 9 nm sample on SiO_2 66
4.32 Heating experiment for a 9 nm sample on plasma etched SiO_2 67
4.33 Heating experiment for a sample on PE 68

5.1 Schematic drawing of the packing of Tyrian purple in the bulk and on substrates 70

List of Tables

1.1 Crystal bulk structure of Tyrian purple 3

3.1 Contact angle measurements of the substrates 32
3.2 Sample overview 33

4.1 XRR for different film thicknesses on SiO_2 43
4.2 Bragg peaks of Tyrian purple on SiO_2 44
4.3 XRR for different film thicknesses on plasma etched SiO_2 . . 48
4.4 Bragg peaks of Tyrian purple on plasma etched SiO_2 50
4.5 Overview of the unit cell parameters of Tyrian purple on different substrates 63

List of Abbrevations

AFM	atomic force microscopy
CVD	chemical vapor deposition
EGDMA	ethylene glycol dimethacrylate
GIXD	grazing incidence X-ray diffraction
HMDSO	hexamethyldisiloxane
iCVD	initiated chemical vapor deposition
PECVD	plasma enhanced chemical vapor deposition
PFDA	1H,1H,2H,2H-perfluorodecyl acrylate
SIP	surface induced phase
XRD	specular X-ray diffraction
XRR	X-ray reflectivity

Bibliography

[1] E. D. Głowacki et al. Natural and nature-inspired semiconductors for organic electronics. *Proceedings of the SPIE* (2011), 81180.

[2] M. Irimia-Vladu et al. Indigo - a natural pigment for high performance ambipolar organic field effect transistors and circuits. *Advanced materials* 24 (2012), 375–380.

[3] E. D. Głowacki et al. Indigo and Tyrian Purple - From Ancient Natural Dyes to Modern Organic Semiconductors. *Israel Journal of Chemistry* 52 (2012), 540–551.

[4] I. V. Klimovich et al. Design of indigo derivatives as environment-friendly organic semiconductors for sustainable organic electronics. *Journal of Materials Chemistry C* 2 (2014), 7621.

[5] P. Friedländer. Über antiken Purpur. *Zeitschrift für Angewandte Chemie* 22 (1909), 2321–2324.

[6] P. Friedländer, S. Bruckner, and G. Deutsch. Über Brom- und Methoxyderivate des Indigos. *Justus Liebig's Annalen der Chemie* 388 (1912), 23–49.

[7] E. D. Głowacki et al. Ambipolar organic field effect transistors and inverters with the natural material Tyrian Purple. *AIP Advances* 1 (2011), 42132.

[8] P. Süsse and C. Krampe. 6,6'-Dibromo-indigo, a main component of Tyrian purple. *Naturwissenschaften* 66 (1979), 110.

[9] S. Larsen and F. Wätjen. The Crystal and Molecular Structures of Tyrian Purple (6,6'-Dibromoindigotin) and 2,2'-Dimethoxyindigotin. *Acta Chem. Scand A* 34 (1980), 171–176.

[10] A. Pichler. "Crystal Structure Solution from Thin Films". Master's thesis. Graz University of Technology, 2013.

[11] E. Mitscherlich. *Abhl. Akad Berlin* 43 (1823).

[12] C. Weißmantel and C. Hamann. *Grundlagen der Festkörperphysik*. 4th. Heidelberg: Johannes Ambrosius Barth, 1995.

[13] Y. Diao et al. Understanding polymorphism in organic semiconductor thin films through nanoconfinement. *Journal of the American Chemical Society* 136 (2014), 17046–17057.

[14] A. A. Virkar et al. Organic semiconductor growth and morphology considerations for organic thin-film transistors. *Advanced Materials* 22 (2010), 3857–3875.

[15] D. Braga et al. Crystal Polymorphism and Multiple Crystal Forms. *Structure and Bonding* 132 (2009), 25–50.

[16] J. Bernstein. Polymorphism – A Perspective. *Crystal Growth & Design* 11 (2011), 632–650.

[17] J. Bernstein. *Polymorphism in Molecular Crystals*. Vol. 14. International Union of Crystallography monographs on crystallography. Oxford, New York: Oxford University Press, 2002.

[18] J. Fraxedas et al. Polymorphic transformations observed on molecular organic thin films. *Europhysics Letters (EPL)* 48 (1999), 461–467.

[19] H. Muguruma, T. K. Saito, and S. Hotta. Conformational polymorphs in vacuum evaporated thin film of 5,5” ’-bis[(2,2,5,5-tetramethyl-1-aza-2,5-disila-1-cyclopentyl)ethyl]-2,2’:5’,2”:5”,2” ’-quaterthiophene. *Thin Solid Films* 445 (2003), 26–31.

[20] M. Yoneya, M. Kawasaki, and M. Ando. Molecular dynamics simulations of pentacene thin films. *Journal of Materials Chemistry* 20 (2010), 10397.

[21] B. Wedl et al. Crystallisation kinetics in thin films of dihexylterthiophene. *RSC Advances* 2 (2012), 4404.

[22] S. Schiefer et al. Determination of the crystal structure of substrate-induced pentacene polymorphs in fiber structured thin films. *Journal of the American Chemical Society* 129 (2007), 10316–10317.

[23] C. Kittel. *Introduction to Solid State Physics*. 8. ed. Hoboken, NJ: Wiley, 2005.

[24] D. W. Bennett. *Understanding single-crystal X-ray crystallography*. Weinheim: Wiley-VCH-Verl., 2010.

[25] M. Birkholz. *Thin film analysis by X-Ray scattering*. 1st. Weinheim: WILEY-VCH, 2006.

[26] D. Schwarzenbach. *Crystallography*. Reprint. Chichester: Wiley, 1997.

[27] R. Resel. "X-ray physics". Lecture notes. Graz University of Technology, 2014.

[28] A. L. Patterson. A Fourier Series Method for the Determination of the Components of Interatomic Distances in Crystals. *Physical Review* 46 (1934), 372–376.

[29] S. Plimpton. Fast Parallel Algorithms for Short-Range Molecular Dynamics. *Journal of Computational Physics* 117 (1995), 1–19.

[30] S. J. Clark et al. First principles methods using CASTEP. *Zeitschrift für Kristallographie* 220 (2005).

[31] H. Sitter et al. Hot-wall-epitaxy - the method of choice for the growth of highly ordered organic epilayers. *Molecular Crystals and Liquid Crystals* 385 (2002), 51–60.

[32] T. Mitsunaga. X-ray thin-film measurement techniques. *The Rigaku Journal* 25 (2009).

[33] P. Scherrer. Bestimmung der Größe und der inneren Struktur von Kolloidteilchen mittels Röntgenstrahlen. *Nachrichten von der Gesellschaft der Wissenschaften zu Göttingen, Mathematisch-Physikalische Klasse* 1918 (1918), 98–100.

[34] J. A. Prins. Über die Dispersion und Absorption von Röntgenstrahlen. *Z. Physik (Zeitschrift für Physik)* 47 (1928), 479–498.

[35] H. Kiessig. Interferenz von Röntgenstrahlen an dünnen Schichten. *Annalen der Physik* 402 (1931), 769–788.

[36] L. G. Parratt. Surface Studies of Solids by Total Reflection of X-Rays. *Physical Review* 95 (1954), 359–369.

[37] S. M. Danauskas et al. Stochastic fitting of specular X-ray reflectivity data using StochFit. *Journal of Applied Crystallography* 41 (2008), 1187–1193.

[38] O. Werzer and R. Resel. Model-Independent X-ray Reflectivity Fitting for Structure Analysis of Poly(3-hexylthiophene) Films. *Macromolecules* 46 (2013), 3529–3533.

[39] I. K. Robinson and D. J. Tweet. Surface X-ray diffraction. *Reports on Progress in Physics* 55 (1992), 599–651.

[40] A. M. Coclite et al. 25th anniversary article: CVD polymers: a new paradigm for surface modification and device fabrication. *Advanced Materials* 25 (2013), 5392–5423.

[41] K. Gleason, ed. *CVD Polymers*. Weinheim: WILEY-VCH, 2015.

[42] C. Ranacher. "Deposition and Characterization of Proton Conductive Polymers by initiated Chemical Vapor Deposition". Master's thesis. Graz University of Technology, 2014.

[43] G. Urstöger. "Characterization of Proton Exchange Membranes produced by Plasma Enhanced Chemical Vapor Deposition". Master's thesis. Graz University of Technology, 2014.

[44] D. K. Owens and R. C. Wendt. Estimation of the surface free energy of polymers. *Journal of Applied Polymer Science* 13 (1969), 1741–1747.

[45] W. A. Zisman. Influence of constitution on adhesion. *Industrial & Engineering Chemistry* 55 (1963), 18–38.

[46] F. M. Fowkes. Attractive forces at interfaces. *Industrial & Engineering Chemistry* 56 (1964), 40–52.

[47] N. A. Geisse. AFM and combined optical techniques. *Materials Today* 12 (2009), 40–45.

[48] A. Neuhold et al. X-ray based tools for the investigation of buried interfaces in organic electronic devices. *Organic electronics* 14 (2013), 479–487.

[49] A. M. Coclite, Y. Shi, and K. K. Gleason. Controlling the Degree of Crystallinity and Preferred Crystallographic Orientation in Poly-Perfluorodecylacrylate Thin Films by Initiated Chemical Vapor Deposition. *Advanced Functional Materials* 22 (2012), 2167–2176.

[50] S. Choi et al. Effect of oxygen plasma treatment on anodic bonding. *Journal of the Korean Physical Society* 38 (2001), 207–209.

[51] B. Lang. "Oberflächenenergie von 100 Silizium-Wafern nach O_2 Plasmabehandlung". Bachelor thesis. Graz University of Technology, 2012.

[52] B. Scherwitzl, R. Resel, and A. Winkler. Film growth, adsorption and desorption kinetics of indigo on SiO2. *The Journal of chemical physics* 140 (2014), 184705.

[53] P. Debye and P. Scherrer. Interferenzen an regellos orientierten Teilchen im Röntgenlicht. I. *Nachrichten von der Gesellschaft der Wissenschaften zu Göttingen, Mathematisch-Physikalische Klasse* (1916), 1–15.

[54] V. A. Gritsenko. Atomic structure of the amorphous nonstoichiometric silicon oxides and nitrides. *Physics-Uspekhi* 51 (2008), 699–708.

[55] R. S. Rowland and R. Taylor. Intermolecular Nonbonded Contact Distances in Organic Crystal Structures: Comparison with Distances Expected from van der Waals Radii. *J. Phys. Chem.* 100 (1996), 7384–7391.

[56] M. L. Główka, D. Martynowski, and K. Kozłowska. Stacking of six-membered aromatic rings in crystals. *Journal of Molecular Structure* 474 (1999), 81–89.